

Elasto-acoustic wave propagation in geophysical media using hybrid high-order methods on general meshes

Romain Mottier[†], Alexandre Ern[‡], Laurent Guillot[§],

Abstract

Hybrid high-order (HHO) methods are numerical methods characterized by several interesting properties such as local conservativity, geometric flexibility and high-order accuracy. Here, HHO schemes are studied for the space semi-discretization of coupled elasto-acoustic waves in the time domain using a first-order formulation. Explicit and singly diagonal implicit Runge–Kutta (ERK & SDIRK) schemes are used for the time discretization. We show that an efficient implementation of explicit (resp. implicit) time schemes calls for a static condensation of the face (resp. cell) unknowns. Crucially, both static condensation procedures only involve block-diagonal matrices. Then, we provide numerical estimates for the CFL stability limit of ERK schemes and present a comparative study on the efficiency of explicit versus implicit schemes. Our findings indicate that implicit time schemes remain competitive in many situations. Finally, simulations in a 2D realistic geophysical configuration are performed, illustrating the geometrical flexibility of the HHO method: both hybrid (triangular and quadrangular) and nonconforming (with hanging nodes) meshes are easily handled, delivering results of comparable accuracy to a reference spectral element software based on tensorized elements.

Mathematics Subjects Classification. 65M12, 65M60, 74J10, 74S05, 35L05.

Keywords. Hybrid high-order methods (HHO), Elasto-acoustic coupling, Wave equations, Runge–Kutta schemes, Efficient implementation, General meshes.

1 Introduction

The accurate computation of mechanical wave propagation is crucial in numerous scientific fields, such as medical imaging [52], non-destructive testing [37], or geophysics [36]. In geophysics for instance, seismic (*i.e.*, elastic), hydroacoustic or infrasonic waves are used to probe the Earth at the local (petroleum and marine exploration) and global scales. Owing to a broad suite of recording instruments deployed in various Earth’s environments, these wavefields jointly provide insights into the Earth’s internal structure [29], seismic source properties, or help monitoring natural hazards [4]. The success of these endeavors strongly depends on the ability to compute and understand how an elasto-acoustic wavefield propagates through media that are heterogeneous and different in nature (solid, fluid). Closed-form or semi-analytical solutions are available only for the simplest geometrical configurations [1], while asymptotic methods often rely on assumptions that may not be fulfilled in more complex scenarios (*e.g.*, ray theory or single-scattering approximations). Consequently, numerical methods that accurately simulate the partial differential equations describing elasto-acoustic waves are required to simulate wave propagation in realistic media of complex geometry.

Advances in high-performance computing have triggered the emergence of various numerical methods. The finite difference method (FDM) is still widely used [44], evolving from regular-grid to staggered-grid approaches with improved accuracy [54]. Despite its efficiency on rectilinear meshes, FDM has long struggled with complex geometries and strong material contrasts. Extensions to

[†]CEA, DAM, DIF, F-91297 Arpajon, France and CERMICS, ENPC, Institut Polytechnique de Paris, F-77455 Marne-la-Vallée cedex 2, and Centre Inria de Paris, 48 rue Barrault, CS 61534, F-75647 Paris, France. Email address: romain.mottier@enpc.fr

[‡]CERMICS, ENPC, Institut Polytechnique de Paris, F-77455 Marne-la-Vallée cedex 2, and Centre Inria de Paris, 48 rue Barrault, CS 61534, F-75647 Paris, France. E-mail address: alexandre.ern@enpc.fr

[§]CEA,DAM, DIF, F-91297 Arpajon, France. Email address: laurent.guillot@cea.fr

more intricate domains have been developed [48], but requiring an increased computational effort. Additionally, higher-order FDM introduce larger stencils, negatively impacting parallel scalability.

A natural alternative to FDM are continuous finite element methods (FEM), which accommodate unstructured meshes and intricate boundaries. However, low-order FEM is computationally inefficient [39], and its high-order extension can suffer from aliasing issues. The spectral element method (SEM), introduced in [47] for fluid dynamics and later adapted to time-domain wave equations [34], leverages the accuracy of spectral methods owing to high-order polynomial approximations based on Lagrangian basis functions whose nodes coincide with the tensorized Gauss-Lobatto-Legendre (GLL) quadrature points. This choice ensures a diagonal mass matrix and efficient explicit time-stepping while retaining high-order accuracy. SEM have been successfully applied to coupled elasto-acoustic wave propagation [33, 10] with a description of the fluid velocity using a potential field. However, SEM essentially relies on a space discretization with quadrilateral/hexahedral elements, which poses meshing challenges for realistic 3D applications. Different extensions to simplicial meshes [18, 42] have demonstrated good dispersion properties [41], yet they may introduce additional computational overheads, difficulties in increasing the order of accuracy, or a loss of mass matrix diagonalization [42]. Moreover, handling severe wavespeed discontinuities necessitates multiscale discretizations in space (nonconforming meshes with h - or p -adaptivity) or time (multiple-time stepping), leading to increased algorithmic complexity, higher computational costs [8], and potential instabilities [25].

These limitations have sparked interest in discontinuous methods, such as finite volume (FV) and discontinuous Galerkin (dG) methods. Both methods rely on local information exchanges through fluxes at mesh interfaces, thereby relaxing the classical FEM C^0 -continuity constraint, and accommodating more naturally meshes with hanging nodes for instance. Some dG methods adopt a second-order formulation in time (*e.g.*, interior penalty methods [30, 20, 2]), whereas others (including FV) adopt a first-order formulation in time, solving for both primal (pressure in acoustics, velocity in elastodynamics) and dual (velocity in acoustics, stress in elastodynamics) variables. Several dG variants exist, depending on the fluxes (some based on Godunov-type upwind fluxes [26, 55], others on central fluxes [43] or modified upwind [56]) and on the polynomial setting (*e.g.*, dG-SEM combinations [55, 3]). While dG methods achieve FEM-like convergence rates, their high computational costs due to the substantial amount of degrees of freedom generally remain a drawback.

Thus, there is room for alternative numerical strategies. Among others, like the Distributional Finite-Difference Method (DFDM) [40], or the Virtual Element Method (VEM) [19], one promising approach is the family of hybrid nonconforming methods, which leverage ideas from both FEM and dG. Hybrid nonconforming methods can achieve higher-order accuracy through a consistent gradient reconstruction based on an additional unknown field defined on the mesh skeleton, hence the term "hybrid". Compared to dG methods, hybrid nonconforming methods have several advantages: (i) They include a built-in and robust stabilization that is less sensitive to parameter tuning than the one used in dG methods; (ii) In the context of elliptic problems, they achieve H^1 -convergence of order $(k + 1)$ and L^2 -convergence of order $(k + 2)$, *i.e.* one order higher than dG methods. For the wave equation in first-order form, they can achieve L^2 -convergence of order $(k + 2)$ under a post-processing for the primal variable [17] (although it may be insufficient in elastodynamics [53]). Moreover, these methods allow for a natural enforcement of coupling conditions by means of the unknowns attached to the mesh skeleton.

The most salient exemple of hybrid nonconforming method is the Hybridizable dG method (HDG). This method was first proposed in [46] for the wave equation in first-order form, following the seminal work [16] on HDG methods for elliptic problems (see also [15] for a second-order formulation in time). HDG methods allow for efficient implicit time-stepping by leveraging static

condensation (*i.e.* the local elimination of the cell unknowns). Efficient explicit time-stepping is also possible whenever the stabilization bilinear form leads to a block-diagonal face-face matrix. Explicit and implicit HDG schemes for the wave equation are compared in [35], where explicit schemes were found more efficient for various configurations. Different conclusions are drawn in the present work, allowing at least to say that the explicit and implicit approaches are both relevant.

Another compelling instance in the class of hybrid nonconforming methods is the Hybrid High-Order (HHO) method. The HHO method approximates the solution within the mesh cells and its trace on the mesh skeleton, both by polynomial unknowns. The setting is of equal-order when the cell and face polynomials are of the same order $k \geq 0$, whereas the setting is of mixed-order when the cell polynomials are one order higher than the face polynomials. The two devising principles of HHO methods are: (i) a gradient reconstruction in each mesh cell from the local cell and face unknowns; (ii) a stabilization that weakly enforces locally the matching of the trace of the cell unknowns with the corresponding face unknowns. Although the devising principles in HHO differ from those in HDG, it has been shown in [14] (see also [13]) that tight connections exist between both approaches, as well as with other hybrid nonconforming methods such as Weak Galerkin and nonconforming VEM. HHO methods were introduced in [23] for linear elasticity and in [24] for linear diffusion. Since then, HHO methods have been applied to a broad range of problems. We refer the reader to the two textbooks [13, 22] and to [6, 7, 51] for the development of HHO methods applied to the (purely) acoustic or elastic wave equation in first- and second-order form (see also [28, 27] for further analysis results).

The approximation of coupled elasto-acoustic waves using HHO methods in space and Runge–Kutta (RK) schemes in time has been started in [45]. Therein, the devising principles of the method were established, and an error analysis in the space semi-discrete setting was proposed. Moreover, numerical results, mostly on academic test cases, were presented to showcase the stability and accuracy properties of the proposed method. Let us briefly summarize the main findings. On the one hand, if explicit RK (ERK) time-stepping schemes are considered, it is recommended to scale the stabilization by an $\mathcal{O}(1)$ -weight (to alleviate the CFL restriction) and to use a plain Least-Squares stabilization. Because of this, it is natural to consider an equal-order setting for the cell and face unknowns. On the other hand, for implicit RK (IRK) schemes, one can consider tighter stabilizations to obtain higher-order convergence rates. Namely, one can scale the stabilization by an $\mathcal{O}(\frac{1}{h})$ -weight (where h is the mesh size) and employ any of the high-order HHO stabilization operators. As discussed in [12] for elliptic problems, the mixed-order setting with Lehrenfeld–Schöberl stabilization appears to be more computationally effective.

In this work, we further develop the above methodology, addressing important computational aspects and assessing the approach on more realistic geophysical settings. The HHO formulations for the explicit and implicit time schemes are those discussed above. Our first main contribution in the paper is to recast the fully discrete problem in algebraic form, so as to show that an efficient implementation of implicit (resp. explicit) time schemes calls for a static condensation of the cell (resp. face) unknowns. Crucially, both static condensation procedures only involve block-diagonal matrices. Our second main contribution is to estimate numerically the CFL stability limit for explicit time schemes and to provide a comparative study on the efficiency of explicit versus implicit time schemes. This is performed on test cases with manufactured solutions and in bilayered problems with an initial Ricker wavelet. As mentioned above, our findings indicate that implicit time schemes remain competitive in many situations. Our third main contribution is to consider a realistic test case including waves trapped in a sedimentary basin, and to show that the proposed methodology delivers accurate solutions, while offering the capability of handling general meshes with hanging nodes. Reference solutions for this latter test case are obtained using a spectral element software using tensorized elements.

The paper is organized as follows. Section 2 introduces the coupled elasto-acoustic model and presents its first-order weak formulation. Section 3 presents the HHO space semi-discretization. Section 4 describes the fully discrete problem, incorporating both explicit and implicit RK schemes and showing the relevance of static condensation procedures in both cases. Section 5 (i) investigates numerically the CFL stability limit for ERK and compared the efficiency (error vs. CPU time) of both explicit and implicit time schemes ; (ii) verifies the accuracy of the proposed methodology on a Ricker wavelet test case (with realistic material properties) for which a semi-analytical solution is available, and performs a further comparative study of explicit vs. implicit time schemes; (iii) showcases the performances of the proposed method on a two-dimensional test case inspired by recent seismoacoustic observations, focusing on the emission of acoustic energy due to the interaction between seismic waves and a sedimentary basin [32, 5]. Numerical results obtained on quadrilateral, simplicial, hybrid, and nonconforming meshes (with hanging nodes) are compared to those produced by a reference spectral element solver based on tensorized elements, thus highlighting the versatility of the HHO method to handle general meshes in complex geological media.

2 Model problem

This section presents the model problem. We use boldface (resp. blackboard) fonts for vectors (resp. tensors), and for vector-valued (resp. tensor-valued) fields and spaces composed of such fields. For a bounded and uniformly positive weight κ , we define the κ -weighted L^2 -inner product as $(u, v)_{L^2(\kappa; \Omega)} := \int_{\Omega} \kappa u v \, d\Omega$ for all $u, v \in L^2(\Omega)$. A similar notation is used for inner products involving vector- and tensor-valued fields.

2.1 Strong formulation

Let $J := (0, T_f)$ denotes the time interval of interest, where $T_f > 0$ represents the final time, and let Ω be a polyhedral domain (open, bounded, connected, Lipschitz set) in \mathbb{R}^d , with $d \in \{2, 3\}$. We partition Ω into two disjoint, polyhedral subdomains, Ω^F and Ω^S (of boundaries $\partial\Omega^F$ and $\partial\Omega^S$), representing the solid and fluid media, respectively. These subdomains share the interface $\Gamma := \partial\Omega^F \cap \partial\Omega^S$, and the unit normal vector \mathbf{n}_Γ on Γ conventionally points from Ω^S to Ω^F . A simplified representation of this setting is displayed in Figure 1 illustrating the geophysical application considered in Section 5.

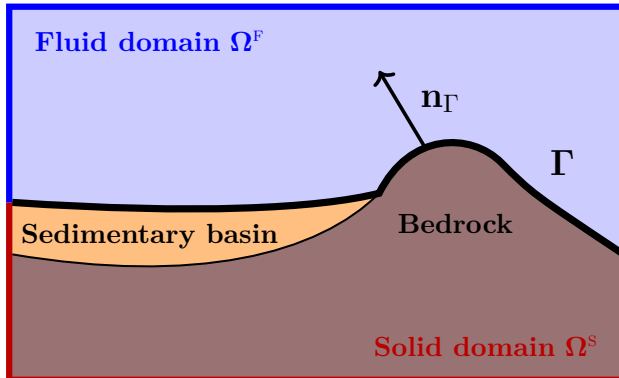


Fig. 1: Solid subdomain Ω^S composed of the sedimentary basin and the bedrock, fluid subdomain Ω^F , and unit normal \mathbf{n}_Γ along the interface Γ (highlighted with a thick black line)

The linear acoustic wave propagation is defined by the evolution of its scalar pressure field p [Pa] and velocity field \mathbf{m} [$\frac{\text{m}}{\text{s}}$], which are described by the following system of partial differential

equations in $J \times \Omega^F$:

$$\rho^F \partial_t \mathbf{m} - \nabla p = \mathbf{0}, \quad (2.1a)$$

$$\frac{1}{\kappa} \partial_t p - \nabla \cdot \mathbf{m} = f^F, \quad (2.1b)$$

where $\rho^F \left[\frac{\text{kg}}{\text{m}^3} \right]$ is the fluid density, $\kappa [\text{Pa}]$ is the fluid bulk modulus, and $f^F [\text{Hz}]$ is the source term. The equation (2.1b) is derived by considering a perfect fluid, where the stress tensor is given by $\mathbf{s}^F := p \mathbb{I} d$, instead of the classical convention $\mathbf{s}^F := -p \mathbb{I} d$, where $\mathbb{I} d$ is the identity tensor. The material properties ρ^F and κ are typically piecewise constant in Ω^F , although it is not mandatory (they can smoothly evolve in space). The speed of the acoustic waves is given by $c_p^F := \sqrt{\kappa / \rho^F} \left[\frac{\text{m}}{\text{s}} \right]$. The initial conditions are specified as $p(0) = p_0$ and $\mathbf{m}(0) = \mathbf{m}_0$ with initial data p_0 and \mathbf{m}_0 .

Let $\nabla_{\text{sym}} := \frac{1}{2}(\nabla + \nabla^\dagger)$ denote the symmetric gradient operator. The elastic wave equations, which describe the evolution of the linearized Cauchy stress tensor $\mathbf{s} [\text{Pa}]$ and the velocity field $\mathbf{v} \left[\frac{\text{m}}{\text{s}} \right]$, consist of the following partial differential equations in $J \times \Omega^S$:

$$\mathbb{C}^{-1} \partial_t \mathbf{s} - \nabla_{\text{sym}} \mathbf{v} = \mathbf{0}, \quad (2.2a)$$

$$\rho^S \partial_t \mathbf{v} - \nabla \cdot \mathbf{s} = \mathbf{f}^S, \quad (2.2b)$$

where $\rho^S \left[\frac{\text{kg}}{\text{m}^3} \right]$ is the solid density, $\mathbb{C} [\text{Pa}]$ is the fourth-order Hooke tensor, and $\mathbf{f}^S \left[\frac{\text{N}}{\text{m}^3} \right]$ is the source term. The material properties \mathbb{C} and ρ^S can be considered piecewise constant in Ω^S . In the framework of isotropic elasticity, \mathbb{C} depends on the Lamé parameters $\lambda [\text{Pa}]$ and $\mu [\text{Pa}]$ as $\mathbb{C}_{ijkl} := \lambda \delta_{ij} \delta_{kl} + \mu (\delta_{ik} \delta_{jl} + \delta_{il} \delta_{jk})$, for all $i, j, k, l \in \{1, \dots, d\}$, where δ is the Kronecker symbol. This setting gives rise to two wave speeds $\left[\frac{\text{m}}{\text{s}} \right]$ corresponding to two types of body waves, far from material interfaces:

$$c_p^S := \sqrt{(\lambda + 2\mu) / \rho^S} \quad \text{for compressional (P-) waves,} \quad (2.3a)$$

$$c_s^S := \sqrt{\mu / \rho^S} \quad \text{for shear (S-) waves.} \quad (2.3b)$$

We do not consider the incompressible limit where $\frac{\lambda}{\mu} \gg 1$, so that the two wave speeds in (2.3) are expected to be of similar magnitude. The initial conditions are specified as $\mathbf{v}(0) = \mathbf{v}_0$ and $\mathbf{s}(0) = \mathbf{s}_0$, with initial data \mathbf{v}_0 and \mathbf{s}_0 .

For simplicity, we impose homogeneous Dirichlet boundary conditions on p on $\partial\Omega^F \setminus \Gamma$ and on \mathbf{v} on $\partial\Omega^S \setminus \Gamma$, which lead to perfect wave reflection at the domain boundaries. The computational domain and time are chosen appropriately, so as to avoid any spurious reflection that could interfere with the main phenomena we want to simulate.

The interface conditions on $J \times \Gamma$ are expressed as follows:

$$\mathbf{v} \cdot \mathbf{n}_\Gamma = \mathbf{m} \cdot \mathbf{n}_\Gamma, \quad (2.4a)$$

$$\mathbf{s} \cdot \mathbf{n}_\Gamma = p \mathbf{n}_\Gamma, \quad (2.4b)$$

where the first equation enforces the continuity of the normal velocity component across the interface (kinematic condition on a perfect fluid-solid boundary where tangential slip is allowed, but there is no separation or interpenetration), and the second equation (dynamic condition) expresses the balance of forces.

2.2 Weak formulation

We define the following functional spaces:

$$\mathbf{M}^F := \mathbf{L}^2(\Omega^F), \quad P^F := \left\{ p \in H^1(\Omega^F) : p|_{\partial\Omega^F \setminus \Gamma} = 0 \right\}, \quad (2.5a)$$

$$\mathbf{S}^S := \mathbb{L}_{\text{sym}}^2(\Omega^S), \quad \mathbf{V}^S := \left\{ \mathbf{v} \in \mathbf{H}^1(\Omega^S) : \mathbf{v}|_{\partial\Omega^S \setminus \Gamma} = \mathbf{0} \right\}. \quad (2.5b)$$

The coupled elasto-acoustic wave problem then consists of finding $(\mathbf{m}, p) : J \rightarrow \mathbf{M}^F \times P^F$ and $(\mathbf{s}, \mathbf{v}) : J \rightarrow \mathbb{S}^S \times \mathbf{V}^S$ such that, for all $t \in J$, the following weak equations hold:

i) For the acoustic wave equations, for all test functions $(\mathbf{r}, q) \in \mathbf{M}^F \times P^F$,

$$(\partial_t \mathbf{m}(t), \mathbf{r})_{L^2(\rho^F; \Omega^F)} - (\nabla p(t), \mathbf{r})_{L^2(\Omega^F)} = 0, \quad (2.6a)$$

$$(\partial_t p(t), q)_{L^2(\frac{1}{\kappa}; \Omega^F)} + (\mathbf{m}(t), \nabla q)_{L^2(\Omega^F)} + (\mathbf{v}(t) \cdot \mathbf{n}_\Gamma, q)_{L^2(\Gamma)} = (f^F(t), q)_{L^2(\Omega^F)}. \quad (2.6b)$$

ii) For the elastic wave equations, for all test functions $(\mathbf{b}, \mathbf{w}) \in \mathbb{S}^S \times \mathbf{V}^S$,

$$(\partial_t \mathbf{s}(t), \mathbf{b})_{\mathbb{L}^2(\mathbb{C}^{-1}; \Omega^S)} - (\nabla_{\text{sym}} \mathbf{v}(t), \mathbf{b})_{\mathbb{L}^2(\Omega^S)} = 0, \quad (2.7a)$$

$$(\partial_t \mathbf{v}(t), \mathbf{w})_{L^2(\rho^S; \Omega^S)} + (\mathbf{s}(t), \nabla_{\text{sym}} \mathbf{w})_{\mathbb{L}^2(\Omega^S)} - (p(t) \mathbf{n}_\Gamma, \mathbf{w})_{L^2(\Gamma)} = (\mathbf{f}^S(t), \mathbf{w})_{L^2(\Omega^S)}. \quad (2.7b)$$

The coupling conditions (2.4a) and (2.4b) are directly incorporated into (2.6b) and (2.7b), respectively. Thus, they are weakly imposed.

3 HHO space semi-discretization

In this section, we introduce a simple description of the space semi-discretization of (2.6)-(2.7) in the HHO framework. Namely, we take a quick look at the way the method deals with general meshes, and how (2.6)-(2.7) are approximated with HHO operators. Our goal is to provide the set of ODEs that drive the time-evolution of the space semi-discrete system in algebraic form, using a generic choice for the local polynomial bases.

3.1 Mesh

Let \mathcal{T} be a polygonal mesh of the domain Ω , constructed so as to align with the partition of Ω into the subdomains Ω^F and Ω^S . The mesh cells are supposed to have planar faces, constructed so as to align with the different boundaries of the subdomains Ω^F and Ω^S . Thus, we generate a piecewise affine approximation of the interface Γ and of the subdomains Ω^S and Ω^F . We assume that the mesh is fine enough to neglect the geometric error introduced by this approximation. Consistently with this assumption, we also assume that all material properties are piecewise constant on \mathcal{T} . For latter use, we define the two sub-meshes, \mathcal{T}^F and \mathcal{T}^S , which cover exactly the subdomains Ω^F and Ω^S , respectively.

The set of mesh faces \mathcal{F} is partitioned as $\mathcal{F} := \mathcal{F}^\circ \cup \mathcal{F}^\partial$, where \mathcal{F}° collects all the interior faces, including those lying on the interface Γ , and \mathcal{F}^∂ collects all the boundary faces on $\partial\Omega$. The set of interior faces is further split as $\mathcal{F}^\circ := \mathcal{F}^{\circ F} \cup \mathcal{F}^{\circ S} \cup \mathcal{F}^\Gamma$, whereas the set of boundary faces is split as $\mathcal{F}^\partial := \mathcal{F}^{\partial F} \cup \mathcal{F}^{\partial S}$, with obvious notation. To simplify later expressions, we define $\mathcal{F}^F := \mathcal{F}^{\circ F} \cup \mathcal{F}^{\partial F} \cup \mathcal{F}^\Gamma$ and $\mathcal{F}^S := \mathcal{F}^{\circ S} \cup \mathcal{F}^{\partial S} \cup \mathcal{F}^\Gamma$ for the sets of faces lying in $\overline{\Omega^F}$ and $\overline{\Omega^S}$, respectively.

We consider general meshes which can contain hanging nodes (see Figure 2). These meshes can be handled in a seamless fashion by any discretization method supporting polyhedral cells, as HHO and dG methods. For instance, in the example shown in Figure 2, elements sharing an edge with the solid-fluid interface and containing hanging nodes from the other mesh (filled elements) are no longer considered as triangles in the fluid region or as quadrilaterals in the solid region, but are treated as quadrilaterals and hexagons, respectively. This approach greatly simplifies the meshing of the domain, particularly at the fluid-solid interface, since it allows for independent meshing of the two subdomains.

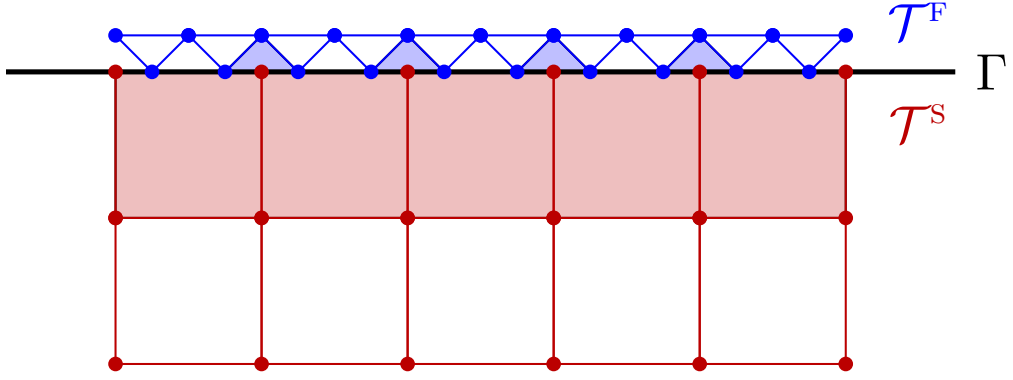


Fig. 2: Generic example of a mesh with hanging nodes at the interface Γ . Filled elements are reinterpreted: filled squares as hexagons and filled triangles as quadrilaterals. Unfilled elements are treated for what they are: squares and triangles.

3.2 Degrees of freedom

Recall that the coupled problem (2.6)-(2.7) relies on primal (p and \mathbf{v}) and on dual (\mathbf{m} and \mathbf{s}) variables. Here, the primal variables are discretized using the HHO method, whereas the dual variables are discretized via a standard dG approach. The dG variables are thus piecewise polynomials of degree k (only a cell component), whereas the HHO variables consist of a pair: a cell component and a face component. The cell component is a piecewise polynomial of degree $k' \in \{k, k+1\}$, whereas the face component is a piecewise polynomial of degree k . The HHO discretization is referred to as equal-order when $k' = k$ and as mixed-order when $k' = k+1$. A polynomial degree $k \geq 1$ is required in the solid subdomain to control the rigid body motions [23]. For simplicity, we consider the same polynomial degree k in both subdomains, although it is not mandatory (we can take $k \geq 0$ in the fluid subdomain).

A generic mesh cell is denoted by $T \in \mathcal{T}$, with its diameter h_T , its outward unit normal \mathbf{n}_T , and the set of its boundary faces $\mathcal{F}_{\partial T}$. A generic mesh face is denoted by $F \in \mathcal{F}$. We define the local polynomial spaces $\mathbb{P}_{\text{sym}}^k(T)$, $\mathbf{P}^k(T)$ and $P^k(T)$ (resp. $\mathbf{P}^k(F)$ and $P^k(F)$) as the restrictions to the mesh cell T (resp. the mesh face F) of symmetric tensor-, vector- and scalar-valued d -variate polynomials of degree at most k (resp. $(d-1)$ -variate polynomials of degree at most k). Altogether, we consider the following dofs:

- from a local point of view, we have

$$p_T \in P^{k'}(T), \quad p_{\partial T} \in P^k(\mathcal{F}_{\partial T}) := \bigtimes_{F \in \mathcal{F}_{\partial T}} P^k(F), \quad \mathbf{m}_T \in \mathbf{P}^k(T), \quad \forall T \in \mathcal{T}^F, \quad (3.1a)$$

$$\mathbf{v}_T \in \mathbf{P}^{k'}(T), \quad \mathbf{v}_{\partial T} \in \mathbf{P}^k(\mathcal{F}_{\partial T}) := \bigtimes_{F \in \mathcal{F}_{\partial T}} \mathbf{P}^k(F), \quad \mathbf{s}_T \in \mathbb{P}_{\text{sym}}^k(T), \quad \forall T \in \mathcal{T}^S. \quad (3.1b)$$

- from a global point of view, we have

$$p_{\mathcal{T}^F} \in P^{k'}(\mathcal{T}^F) := \bigtimes_{T \in \mathcal{T}^F} P^{k'}(T), \quad p_{\mathcal{F}^F} \in P^k(\mathcal{F}^F) := \bigtimes_{F \in \mathcal{F}^F} P^k(F), \quad \mathbf{m}_{\mathcal{T}^F} \in \mathbf{M}^k(\mathcal{T}^F) := \bigtimes_{T \in \mathcal{T}^F} \mathbf{P}^k(T), \quad (3.2a)$$

$$\mathbf{v}_{\mathcal{T}^S} \in \mathbf{V}^{k'}(\mathcal{T}^S) := \bigtimes_{T \in \mathcal{T}^S} \mathbf{P}^{k'}(T), \quad \mathbf{v}_{\mathcal{F}^S} \in \mathbf{V}^k(\mathcal{F}^S) := \bigtimes_{F \in \mathcal{F}^S} \mathbf{P}^k(F), \quad \mathbf{s}_{\mathcal{T}^S} \in \mathbb{S}^k(\mathcal{T}^S) := \bigtimes_{T \in \mathcal{T}^S} \mathbb{P}_{\text{sym}}^k(T). \quad (3.2b)$$

In Figure 3, we illustrate the dofs involved in the space discretization of a 2D domain near a solid-fluid interface, for hexagonal meshes and polynomial degrees $k' = k = 1$. There are 9 cell unknowns in each fluid cell (3 for the primal variable and 6 for the dual variable), and there are 2 unknowns for each face $F \in \mathcal{F}^{\text{OF}}$. There are 15 cell unknowns in each solid cell (6 for the primal variable

and 9 for the dual variable), and there are 4 unknowns for each face $F \in \mathcal{F}^{\text{os}}$. Finally, there are 6 unknowns for each face $F \in \mathcal{F}^{\Gamma}$ (2 from the fluid part and 4 from the solid part).

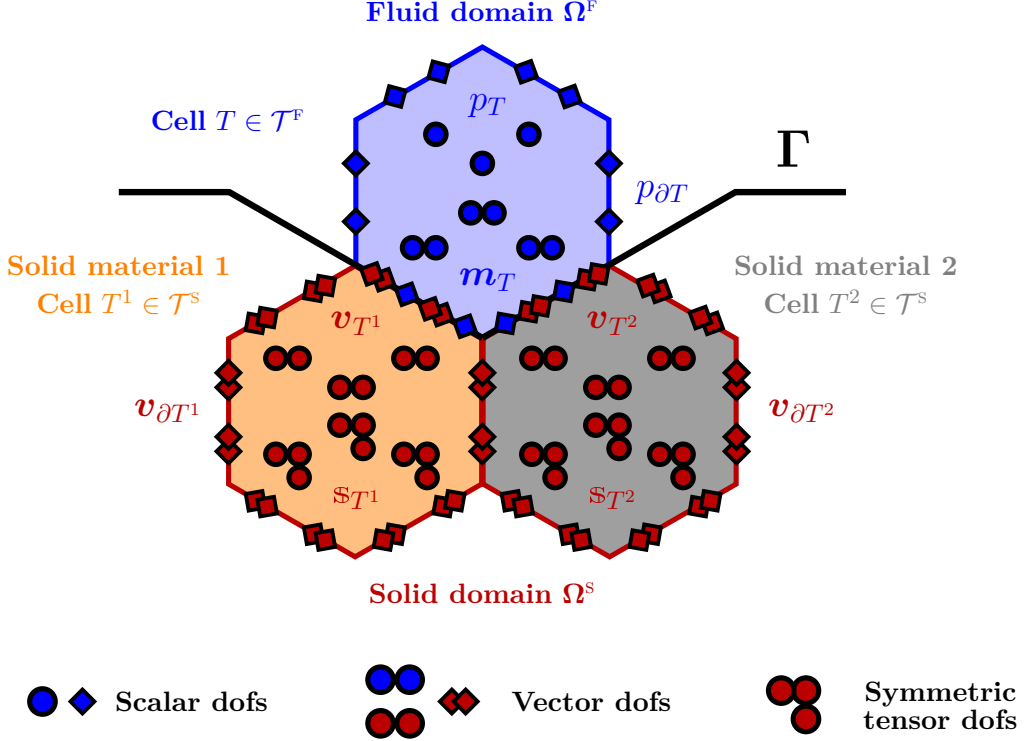


Fig. 3: Elasto-acoustic dofs along a solid-fluid interface, with hexagonal mesh cells and lowest equal-order discretization ($k' = k = 1$).

3.3 Space semi-discrete formulation and algebraic realization

The space semi-discrete formulation of the model problem (2.6)-(2.7) consists in finding $(p_{\mathcal{T}^{\text{F}}}(t), p_{\mathcal{F}^{\text{F}}}(t), \mathbf{m}_{\mathcal{T}^{\text{F}}}(t)) : J \rightarrow P^{k'}(\mathcal{T}^{\text{F}}) \times P^k(\mathcal{F}^{\text{F}}) \times \mathbf{M}^k(\mathcal{T}^{\text{F}})$ in the fluid subdomain and $(\mathbf{v}_{\mathcal{T}^{\text{S}}}(t), \mathbf{v}_{\mathcal{F}^{\text{S}}}(t), \mathbf{s}_{\mathcal{T}^{\text{S}}}(t)) \in \mathbf{V}^{k'}(\mathcal{T}^{\text{S}}) \times \mathbf{V}^k(\mathcal{F}^{\text{S}}) \times \mathbb{S}^k(\mathcal{T}^{\text{S}})$ in the solid subdomain, such that, for all $t \in \bar{J}$,

$$(\partial_t \mathbf{m}_{\mathcal{T}^{\text{F}}}(t), \mathbf{r}_{\mathcal{T}^{\text{F}}})_{\mathbf{L}^2(\rho^{\text{F}}; \Omega^{\text{F}})} - (\mathbf{g}_{\mathcal{T}^{\text{F}}}(p_{\mathcal{T}^{\text{F}}}(t), p_{\mathcal{F}^{\text{F}}}(t)), \mathbf{r}_{\mathcal{T}^{\text{F}}})_{\mathbf{L}^2(\Omega^{\text{F}})} = 0, \quad (3.3a)$$

$$\begin{aligned} & (\partial_t p_{\mathcal{T}^{\text{F}}}(t), q_{\mathcal{T}^{\text{F}}})_{L^2(\frac{1}{\kappa}; \Omega^{\text{F}})} + (\mathbf{m}_{\mathcal{T}^{\text{F}}}(t), \mathbf{g}_{\mathcal{T}^{\text{F}}}(q_{\mathcal{T}^{\text{F}}}, q_{\mathcal{F}^{\text{F}}}))_{\mathbf{L}^2(\Omega^{\text{F}})} \\ & + s^{\text{F}}((p_{\mathcal{T}^{\text{F}}}(t), p_{\mathcal{F}^{\text{F}}}(t)), (q_{\mathcal{T}^{\text{F}}}, q_{\mathcal{F}^{\text{F}}})) + (\mathbf{v}_{\mathcal{F}^{\text{S}}}(t) \cdot \mathbf{n}_{\Gamma}, q_{\mathcal{F}^{\text{F}}})_{L^2(\Gamma)} = (f^{\text{F}}(t), q_{\mathcal{T}^{\text{F}}})_{L^2(\Omega^{\text{F}})}, \end{aligned} \quad (3.3b)$$

for all $\mathbf{r}_{\mathcal{T}^{\text{F}}} \in \mathbf{M}^k(\mathcal{T}^{\text{F}})$ and all $(q_{\mathcal{T}^{\text{F}}}, q_{\mathcal{F}^{\text{F}}}) \in P^{k'}(\mathcal{T}^{\text{F}}) \times P^k(\mathcal{F}^{\text{F}})$, and

$$(\partial_t \mathbf{s}_{\mathcal{T}^{\text{S}}}(t), \mathbf{b}_{\mathcal{T}^{\text{S}}})_{\mathbb{L}^2(\mathbb{C}^{-1}; \Omega^{\text{S}})} - (\mathbf{g}_{\mathcal{T}^{\text{S}}}^{\text{sym}}(\mathbf{v}_{\mathcal{T}^{\text{S}}}(t), \mathbf{v}_{\mathcal{F}^{\text{S}}}(t)), \mathbf{b}_{\mathcal{T}^{\text{S}}})_{\mathbb{L}^2(\Omega^{\text{S}})} = 0, \quad (3.4a)$$

$$\begin{aligned} & (\partial_t \mathbf{v}_{\mathcal{T}^{\text{S}}}(t), \mathbf{w}_{\mathcal{T}^{\text{S}}})_{\mathbf{L}^2(\rho^{\text{S}}; \Omega^{\text{S}})} + (\mathbf{s}_{\mathcal{T}^{\text{S}}}(t), \mathbf{g}_{\mathcal{T}^{\text{S}}}^{\text{sym}}(\mathbf{w}_{\mathcal{T}^{\text{S}}}, \mathbf{w}_{\mathcal{F}^{\text{S}}}))_{\mathbb{L}^2(\Omega^{\text{S}})} \\ & + s^{\text{S}}((\mathbf{v}_{\mathcal{T}^{\text{S}}}(t), \mathbf{v}_{\mathcal{F}^{\text{S}}}(t)), (\mathbf{w}_{\mathcal{T}^{\text{S}}}, \mathbf{w}_{\mathcal{F}^{\text{S}}})) - (p_{\mathcal{F}^{\text{F}}}(t) \mathbf{n}_{\Gamma}, \mathbf{w}_{\mathcal{F}^{\text{S}}})_{\mathbf{L}^2(\Gamma)} = (\mathbf{f}^{\text{S}}(t), \mathbf{w}_{\mathcal{T}^{\text{S}}})_{\mathbf{L}^2(\Omega^{\text{S}})}, \end{aligned} \quad (3.4b)$$

for all $\mathbf{b}_{\mathcal{T}^{\text{S}}} \in \mathbb{S}^k(\mathcal{T}^{\text{S}})$ and all $(\mathbf{w}_{\mathcal{T}^{\text{S}}}, \mathbf{w}_{\mathcal{F}^{\text{S}}}) \in \mathbf{V}^{k'}(\mathcal{T}^{\text{S}}) \times \mathbf{V}^k(\mathcal{F}^{\text{S}})$. Here, $\mathbf{g}_{\mathcal{T}^{\text{F}}}$, $\mathbf{g}_{\mathcal{T}^{\text{S}}}^{\text{sym}}$, s^{F} , and s^{S} are the global (symmetric) gradient reconstruction operators and global stabilization bilinear forms whose expressions are given by the right-hand sides of equations (3.9)-(3.10) below. The main ideas are the following: the (symmetric) gradient reconstruction allows to consistently and locally build the (symmetric) gradient of the primal variable using both its cell and face dofs; the stabilization bilinear form weakly enforces locally the matching of the trace of the cell dofs with the face dofs. The reader is referred to [45] for further insight into the HHO formulation.

To derive the algebraic realization of (3.3)-(3.4), we consider the following generic bases:

$$\{\varphi_i\}_{1 \leq i \leq N_{\mathcal{T}^F}^{k'}}, \quad \{\psi_i\}_{1 \leq i \leq N_{\mathcal{F}^F}^k}, \quad \{\zeta_k\}_{1 \leq k \leq M_{\mathcal{T}^F}^k}, \quad (3.5a)$$

$$\{\phi_i\}_{1 \leq i \leq L_{\mathcal{T}^S}^{k'}}, \quad \{\theta_i\}_{1 \leq i \leq L_{\mathcal{F}^S}^k}, \quad \{\mathbb{Y}_k\}_{1 \leq k \leq H_{\mathcal{T}^S}^k}, \quad (3.5b)$$

with the corresponding dimensions

$$N_{\mathcal{T}^F}^{k'} := \dim(P^{k'}(\mathcal{T}^F)), \quad N_{\mathcal{F}^F}^k := \dim(P^k(\mathcal{F}^F)), \quad M_{\mathcal{T}^F}^k := \dim(\mathbf{M}^k(\mathcal{T}^F)), \quad (3.6a)$$

$$L_{\mathcal{T}^S}^{k'} := \dim(\mathbf{V}^{k'}(\mathcal{T}^S)), \quad L_{\mathcal{F}^S}^k := \dim(\mathbf{V}^k(\mathcal{F}^S)), \quad H_{\mathcal{T}^S}^k := \dim(\mathbb{S}^k(\mathcal{T}^S)). \quad (3.6b)$$

The basis $\{\zeta_k\}_{1 \leq k \leq M_{\mathcal{T}^F}^k}$ is build by combining Cartesian basis vectors of \mathbb{R}^d with scalar basis functions of $P^k(\mathcal{T}^F)$. Similarly, the bases $\{\phi_i\}_{1 \leq i \leq L_{\mathcal{T}^S}^{k'}}$, $\{\theta_i\}_{1 \leq i \leq L_{\mathcal{F}^S}^k}$ and $\{\mathbb{Y}_k\}_{1 \leq k \leq H_{\mathcal{T}^S}^k}$ are built by combining Cartesian basis vectors of \mathbb{R}^d , \mathbb{R}^d and $\mathbb{R}_{\text{sym}}^{d \times d}$, respectively, with scalar basis functions of $P^{k'}(\mathcal{T}^S)$, $P^k(\mathcal{F}^S)$ and $P^k(\mathcal{T}^S)$, respectively. For all the scalar-valued polynomial spaces, we use a local modal basis composed of monomials centered at the barycenter of the corresponding geometric object.

Degrees of freedom. Let $(P_{\mathcal{T}^F}(t), P_{\mathcal{F}^F}(t)) \in \mathbb{R}^{N_{\mathcal{T}^F}^{k'} \times N_{\mathcal{F}^F}^k}$ and $M_{\mathcal{T}^F}(t) \in \mathbb{R}^{M_{\mathcal{T}^F}^k}$ represent the time-dependent component vectors of $(p_{\mathcal{T}^F}(t), p_{\mathcal{F}^F}(t)) \in P^{k'}(\mathcal{T}^F) \times P^k(\mathcal{F}^F)$ and $\mathbf{m}_{\mathcal{T}}(t) \in \mathbf{M}^k(\mathcal{T}^F)$ in the fluid subdomain Ω^F , respectively. Let $(V_{\mathcal{T}^S}(t), V_{\mathcal{F}^S}(t)) \in \mathbb{R}^{L_{\mathcal{T}^S}^{k'} \times L_{\mathcal{F}^S}^k}$ and $S_{\mathcal{T}^S} \in \mathbb{R}^{H_{\mathcal{T}^S}^k}$ represent the time-dependent component vectors of $(\mathbf{v}_{\mathcal{T}^S}(t), \mathbf{v}_{\mathcal{F}^S}(t)) \in \mathbf{V}^{k'}(\mathcal{T}^S) \times \mathbf{V}^k(\mathcal{F}^S)$ and $\mathbf{s}_{\mathcal{T}^S} \in \mathbb{S}^k(\mathcal{T}^S)$ in the solid subdomain Ω^S , respectively. The algebraic realization of (3.3)-(3.4) is, for all $t \in \bar{J}$,

$$\begin{bmatrix} \mathcal{M}_{\mathcal{T}^F}^{\rho^F} & 0 \\ 0 & \mathcal{M}_{\mathcal{T}^F}^{\frac{1}{\kappa}} \end{bmatrix} \begin{bmatrix} 0 & 0 \\ 0 & 0 \end{bmatrix} + \frac{d}{dt} \begin{bmatrix} M_{\mathcal{T}^F} \\ P_{\mathcal{T}^F} \\ S_{\mathcal{T}^S} \\ V_{\mathcal{T}^S} \\ P_{\mathcal{F}^F} \\ V_{\mathcal{F}^F} \end{bmatrix} = \begin{bmatrix} 0 & \mathcal{G}_{\mathcal{T}^F} & 0 & 0 & \mathcal{G}_{\mathcal{T}^F \mathcal{F}^F} & 0 \\ -\mathcal{G}_{\mathcal{T}^F}^\dagger & \Sigma_{\mathcal{T}^F} & 0 & 0 & \Sigma_{\mathcal{T}^F \mathcal{F}^F} & 0 \\ 0 & 0 & 0 & \mathcal{H}_{\mathcal{T}^S} & 0 & \mathcal{H}_{\mathcal{T}^S \mathcal{F}^S} \\ 0 & 0 & -\mathcal{H}_{\mathcal{T}^S}^\dagger & \Sigma_{\mathcal{T}^S} & 0 & \Sigma_{\mathcal{T}^S \mathcal{F}^S} \\ 0 & 0 & 0 & 0 & \Sigma_{\mathcal{F}^F} & \mathcal{C}_{\mathcal{F}^F} \\ 0 & 0 & 0 & -\mathcal{H}_{\mathcal{T}^S \mathcal{F}^S}^\dagger & -\mathcal{C}_{\mathcal{F}^F}^\dagger & \Sigma_{\mathcal{F}^S} \end{bmatrix} \begin{bmatrix} M_{\mathcal{T}^F} \\ P_{\mathcal{T}^F} \\ S_{\mathcal{T}^S} \\ V_{\mathcal{T}^S} \\ P_{\mathcal{F}^F} \\ V_{\mathcal{F}^F} \end{bmatrix} = \begin{bmatrix} 0 \\ F_{\mathcal{T}^F} \\ 0 \\ F_{\mathcal{T}^S} \\ 0 \\ 0 \end{bmatrix}, \quad (3.7)$$

where the different blocks are defined as follows.

Mass matrices. The mass matrices $\mathcal{M}_{\mathcal{T}^F}^{\rho^F} \in \mathbb{R}^{M_{\mathcal{T}^F}^k \times M_{\mathcal{T}^F}^k}$ and $\mathcal{M}_{\mathcal{T}^F}^{\frac{1}{\kappa}} \in \mathbb{R}^{N_{\mathcal{T}^F}^{k'} \times N_{\mathcal{T}^F}^{k'}}$ are associated with the inner products in $L^2(\rho^F; \Omega^F)$ and $L^2(\frac{1}{\kappa}; \Omega^F)$, respectively, and the mass matrices $\mathcal{M}_{\mathcal{T}^S}^{\mathbb{C}^{-1}} \in \mathbb{R}^{H_{\mathcal{T}^S}^k \times H_{\mathcal{T}^S}^k}$ and $\mathcal{M}_{\mathcal{T}^S}^{\rho^S} \in \mathbb{R}^{L_{\mathcal{T}^S}^{k'} \times L_{\mathcal{T}^S}^{k'}}$ are associated with the inner products in $\mathbb{L}_{\text{sym}}^2(\mathbb{C}^{-1}; \Omega^S)$ and $L^2(\rho^S; \Omega^S)$, respectively. Their (classical) expressions are as follows:

$$\mathcal{M}_{\mathcal{T}^F}^\dagger \mathcal{M}_{\mathcal{T}^F}^{\rho^F} R_{\mathcal{T}^F} = \sum_{T \in \mathcal{T}^F} \rho^F(\mathbf{m}_T, \mathbf{r})_{L^2(T)}, \quad P_{\mathcal{T}^F}^\dagger \mathcal{M}_{\mathcal{T}^F}^{\frac{1}{\kappa}} Q_{\mathcal{T}^F} = \sum_{T \in \mathcal{T}^F} \frac{1}{\kappa} (p_T, q)_{L^2(T)}, \quad (3.8a)$$

$$S_{\mathcal{T}^S}^\dagger \mathcal{M}_{\mathcal{T}^S}^{\mathbb{C}^{-1}} B_{\mathcal{T}^S} = \sum_{T \in \mathcal{T}^S} \mathbb{C}^{-1}(\mathbf{s}_T, \mathbf{b})_{L^2(T)}, \quad V_{\mathcal{T}^S}^\dagger \mathcal{M}_{\mathcal{T}^S}^{\rho^S} W_{\mathcal{T}^S} = \sum_{T \in \mathcal{T}^S} \rho^S(\mathbf{v}_T, \mathbf{w})_{L^2(T)}, \quad (3.8b)$$

for all $\mathbf{m}_{\mathcal{T}^F}, \mathbf{r} \in \mathbf{P}^k(\mathcal{T}^F)$ and all $p_{\mathcal{T}^F}, q \in P^{k'}(\mathcal{T}^F)$ with component vectors $M_{\mathcal{T}^F}$, $R_{\mathcal{T}^F}$ and $P_{\mathcal{T}^F}$, $Q_{\mathcal{T}^F}$, respectively, and all $\mathbf{s}_{\mathcal{T}^S}, \mathbf{b} \in \mathbb{S}^k(\mathcal{T}^S)$ and all $\mathbf{v}_{\mathcal{T}^S}, \mathbf{w} \in \mathbf{V}^{k'}(\mathcal{T}^S)$ with component vectors $S_{\mathcal{T}^S}$, $B_{\mathcal{T}^S}$ and $V_{\mathcal{T}^S}$, $W_{\mathcal{T}^S}$, respectively.

Gradient reconstruction blocks. The gradient reconstruction blocks $\mathcal{G}_{\mathcal{T}^F} \in \mathbb{R}^{M_{\mathcal{T}^F}^k \times N_{\mathcal{T}^F}^{k'}}$ and $\mathcal{G}_{\mathcal{T}^F \mathcal{F}^F} \in \mathbb{R}^{M_{\mathcal{T}^F}^k \times N_{\mathcal{F}^F}^k}$ and the symmetric gradient reconstruction blocks $\mathcal{H}_{\mathcal{T}^S} \in \mathbb{R}^{H_{\mathcal{T}^S}^k \times L_{\mathcal{T}^S}^{k'}}$ and

$\mathcal{H}_{\mathcal{T}^s \mathcal{F}^s} \in \mathbb{R}^{H_{\mathcal{T}^s}^k \times L_{\mathcal{F}^s}^k}$ are defined so that they satisfy

$$(\mathcal{G}_{\mathcal{T}^F} P_{\mathcal{T}^F} + \mathcal{G}_{\mathcal{T}^F \mathcal{F}^F} P_{\mathcal{F}^F})^\dagger R_{\mathcal{T}^F} = \sum_{T \in \mathcal{T}^F} \left\{ (\nabla p_T, \mathbf{r})_{L^2(T)} - (p_T - p_{\partial T}, \mathbf{r} \cdot \mathbf{n}_T)_{L^2(\partial T)} \right\}, \quad (3.9a)$$

$$(\mathcal{H}_{\mathcal{T}^s} V_{\mathcal{T}^s} + \mathcal{H}_{\mathcal{T}^s \mathcal{F}^s} V_{\mathcal{F}^s})^\dagger B_{\mathcal{T}^s} = \sum_{T \in \mathcal{T}^s} \left\{ (\nabla_{\text{sym}} \mathbf{v}_T, \mathbf{b})_{\mathbb{L}_{\text{sym}}^2(T)} - (\mathbf{v}_T - \mathbf{v}_{\partial T}, \mathbf{b} \cdot \mathbf{n}_T)_{L^2(\partial T)} \right\}, \quad (3.9b)$$

for all $(p_{\mathcal{T}^F}, p_{\mathcal{F}^F}) \in P^{k'}(\mathcal{T}^F) \times P^k(\mathcal{F}^F)$, all $(\mathbf{v}_{\mathcal{T}^s}, \mathbf{v}_{\mathcal{F}^s}) \in \mathbf{V}^{k'}(\mathcal{T}^s) \times \mathbf{V}^k(\mathcal{F}^s)$ with component vectors $P_{\mathcal{T}^F}$, $P_{\mathcal{F}^F}$ and $V_{\mathcal{T}^s}$, $V_{\mathcal{F}^s}$, respectively, and for all $\mathbf{r} \in \mathbf{M}^k(\mathcal{T}^F)$, all $\mathbf{b} \in \mathbb{S}^k(\mathcal{T}^s)$ with component vectors $R_{\mathcal{T}^F}$ and $B_{\mathcal{T}^s}$, respectively.

Stabilization blocks. The fluid stabilization blocks $\Sigma_{\mathcal{T}^F} \in \mathbb{R}^{N_{\mathcal{T}^F}^{k'} \times N_{\mathcal{T}^F}^{k'}}$, $\Sigma_{\mathcal{T}^F \mathcal{F}^F} \in \mathbb{R}^{N_{\mathcal{T}^F}^{k'} \times N_{\mathcal{F}^F}^k}$, and $\Sigma_{\mathcal{F}^F} \in \mathbb{R}^{N_{\mathcal{F}^F}^k \times N_{\mathcal{F}^F}^k}$ and the solid stabilization blocks $\Sigma_{\mathcal{T}^s} \in \mathbb{R}^{L_{\mathcal{T}^s}^{k'} \times L_{\mathcal{T}^s}^{k'}}$, $\Sigma_{\mathcal{T}^s \mathcal{F}^s} \in \mathbb{R}^{L_{\mathcal{T}^s}^{k'} \times L_{\mathcal{F}^s}^k}$, and $\Sigma_{\mathcal{F}^s} \in \mathbb{R}^{L_{\mathcal{F}^s}^k \times L_{\mathcal{F}^s}^k}$ are defined so that they satisfy

$$\begin{aligned} & (\Sigma_{\mathcal{T}^F} P_{\mathcal{T}^F} + \Sigma_{\mathcal{T}^F \mathcal{F}^F} P_{\mathcal{F}^F})^\dagger Q_{\mathcal{T}^F} + (\Sigma_{\mathcal{T}^F \mathcal{F}^F}^\dagger P_{\mathcal{T}^F} + \Sigma_{\mathcal{F}^F} P_{\mathcal{F}^F})^\dagger Q_{\mathcal{F}^F} \\ &= \sum_{T \in \mathcal{T}^F} \tau_T^F (S_{\partial T}(p_T, p_{\partial T}), S_{\partial T}(q_T, q_{\partial T}))_{L^2(\partial T)}, \end{aligned} \quad (3.10a)$$

$$\begin{aligned} & (\Sigma_{\mathcal{T}^s} V_{\mathcal{T}^s} + \Sigma_{\mathcal{T}^s \mathcal{F}^s} V_{\mathcal{F}^s})^\dagger W_{\mathcal{T}^s} + (\Sigma_{\mathcal{T}^s \mathcal{F}^s}^\dagger V_{\mathcal{T}^s} + \Sigma_{\mathcal{F}^s} V_{\mathcal{F}^s})^\dagger W_{\mathcal{F}^s} \\ &= \sum_{T \in \mathcal{T}^s} \tau_T^s (S_{\partial T}(\mathbf{v}_T, \mathbf{v}_{\partial T}), S_{\partial T}(\mathbf{w}_T, \mathbf{w}_{\partial T}))_{L^2(\partial T)}, \end{aligned} \quad (3.10b)$$

for all $(p_{\mathcal{T}^F}, p_{\mathcal{F}^F}) \in P^{k'}(\mathcal{T}^F) \times P^k(\mathcal{F}^F)$ and all $(\mathbf{v}_{\mathcal{T}^s}, \mathbf{v}_{\mathcal{F}^s}) \in \mathbf{V}^{k'}(\mathcal{T}^s) \times \mathbf{V}^k(\mathcal{F}^s)$ with component vectors $P_{\mathcal{T}^F}$, $P_{\mathcal{F}^F}$ and $V_{\mathcal{T}^s}$, $V_{\mathcal{F}^s}$, respectively, and for all $(q_{\mathcal{T}^F}, q_{\mathcal{F}^F}) \in P^{k'}(\mathcal{T}^F) \times P^k(\mathcal{F}^F)$ and all $(\mathbf{w}_{\mathcal{T}^s}, \mathbf{w}_{\mathcal{F}^s}) \in \mathbf{V}^{k'}(\mathcal{T}^s) \times \mathbf{V}^k(\mathcal{F}^s)$ with component vectors $Q_{\mathcal{T}^F}$, $Q_{\mathcal{F}^F}$ and $W_{\mathcal{T}^s}$, $W_{\mathcal{F}^s}$, respectively. The stabilization parameters are defined as follows:

$$\tau_T^F := (\rho^F c_P^F)|_T^{-1} \tilde{h}_T^{-\alpha}, \quad \tau_T^s := (\rho^s c^s)|_T \tilde{h}_T^{-\alpha}, \quad (3.11)$$

where the local scaling by $(\rho^F c_P^F)|_T^{-1}$ and $(\rho^s c^s)|_T$ follows from physical consistency, the parameter $\alpha \in \{0, 1\}$ is used to shift from $\mathcal{O}(1)$ -stabilization ($\alpha = 0$) to $\mathcal{O}(\frac{1}{h})$ -stabilization ($\alpha = 1$), and $\tilde{h}_T := \frac{h_T}{\ell_\Omega}$ is a normalized cell diameter, where the global length scale $\ell_\Omega := \text{diam}(\Omega)$ is introduced for dimensional consistency.

Regarding the local stabilization operators $S_{\partial T} : P^{k'}(T) \times P^k(\mathcal{F}_{\partial T}) \rightarrow P^k(\mathcal{F}_{\partial T})$ and $S_{\partial T} : P^{k'}(T) \times \mathbf{P}^k(\mathcal{F}_{\partial T}) \rightarrow \mathbf{P}^k(\mathcal{F}_{\partial T})$, we consider two configurations:

- The first one, which we use in the equal-order HHO discretization ($k' = k$), corresponds to a plain Least-Squares stabilization:

$$S_{\partial T}(p_T, p_{\partial T}) := p_T|_{\partial T} - p_{\partial T}, \quad S_{\partial T}(\mathbf{v}_T, \mathbf{v}_{\partial T}) := \mathbf{v}_T|_{\partial T} - \mathbf{v}_{\partial T}. \quad (3.12)$$

This stabilization will be used with the scaling $\alpha = 0$ and explicit time-stepping schemes.

- The second one, which we use in the mixed-order HHO discretization ($k' = k+1$), corresponds to the Lehrenfeld–Schöberl stabilization [38]:

$$S_{\partial T}(p_T, p_{\partial T}) := \Pi_{\partial T}^k(p_T|_{\partial T}) - p_{\partial T}, \quad S_{\partial T}(\mathbf{v}_T, \mathbf{v}_{\partial T}) := \Pi_{\partial T}^k(\mathbf{v}_T|_{\partial T}) - \mathbf{v}_{\partial T}, \quad (3.13)$$

where $\Pi_{\partial T}^k$ is the local $L^2(\partial T)$ -orthogonal projection onto $P^k(\mathcal{F}_{\partial T})$. This stabilization will be used with the scaling $\alpha = 1$ and implicit time-stepping schemes.

Coupling blocks. The matrix $\mathcal{C}_{\mathcal{F}^\Gamma} \in \mathbb{R}^{N_{\mathcal{F}^F}^k \times L_{\mathcal{F}^S}^k}$ representing the coupling terms is defined so that

$$Q_{\mathcal{F}^\Gamma}^\dagger \mathcal{C}_{\mathcal{F}^\Gamma} V_{\mathcal{F}^S} = (\mathbf{v}_{\mathcal{F}^S} \cdot \mathbf{n}_\Gamma, q_{\mathcal{F}^F})_{L^2(\Gamma)}, \quad (3.14)$$

for all $q_{\mathcal{F}^F} \in P^k(\mathcal{F}^F)$ with component vector $Q_{\mathcal{F}^F} \in \mathbb{R}^{N_{\mathcal{F}^F}^k}$ and all $\mathbf{v}_{\mathcal{F}^S} \in \mathbf{P}^k(\mathcal{F}^S)$ with component vector $V_{\mathcal{F}^S} \in \mathbb{R}^{L_{\mathcal{F}^S}^k}$. Notice that $\mathcal{C}_{\mathcal{F}^\Gamma}$ is block-diagonal with a nonzero block only for all $F \in \mathcal{F}^\Gamma$.

Source terms. The source terms $\mathbf{F}_{\mathcal{T}^F}(t) \in \mathbb{R}^{N_{\mathcal{T}^F}^{k'}}$ and $\mathbf{F}_{\mathcal{T}^S}(t) \in \mathbb{R}^{L_{\mathcal{T}^S}^{k'}}$ are time-dependent and correspond to the algebraic realization of the linear forms

$$\mathbf{F}_{\mathcal{T}^F}^\dagger(t) \mathcal{M}_{\mathcal{T}^F} Q_{\mathcal{T}^F} = \sum_{T \in \mathcal{T}^F} (f^F(t), q)_{L^2(T)}, \quad (3.15a)$$

$$\mathbf{F}_{\mathcal{T}^S}^\dagger(t) \mathcal{M}_{\mathcal{T}^S} W_{\mathcal{T}^S} = \sum_{T \in \mathcal{T}^S} (\mathbf{f}^S(t), \mathbf{w})_{L^2(T)}, \quad (3.15b)$$

for all $q \in P^{k'}(\mathcal{T}^F)$ and all $\mathbf{w} \in \mathbf{P}^{k'}(\mathcal{T}^S)$ with component vectors $Q_{\mathcal{T}^F}$ and $W_{\mathcal{T}^S}$, respectively, and $\mathcal{M}_{\mathcal{T}^F}$ and $\mathcal{M}_{\mathcal{T}^S}$ are the mass matrices associated with the canonical inner products in $L^2(\Omega^F)$ and $L^2(\Omega^S)$, respectively.

Equation (3.7) can be rewritten in a more compact form by regrouping all the cell unknowns on the one hand, and all the face unknowns on the other hand. With obvious notation, we obtain

$$\begin{bmatrix} \mathcal{M}_{\mathcal{T}} & 0 \\ 0 & 0 \end{bmatrix} \partial_t \begin{bmatrix} U_{\mathcal{T}} \\ U_{\mathcal{F}} \end{bmatrix} + \begin{bmatrix} \mathcal{K}_{\mathcal{T}} & \mathcal{K}_{\mathcal{T}\mathcal{F}} \\ \mathcal{K}_{\mathcal{F}\mathcal{T}} & \mathcal{K}_{\mathcal{F}} \end{bmatrix} \begin{bmatrix} U_{\mathcal{T}} \\ U_{\mathcal{F}} \end{bmatrix} = \begin{bmatrix} \mathbf{F}_{\mathcal{T}} \\ 0 \end{bmatrix}, \quad (3.16)$$

where $\mathcal{M}_{\mathcal{T}}$ is the cell mass matrix, $\mathcal{K}_{\mathcal{T}}$, $\mathcal{K}_{\mathcal{T}\mathcal{F}}$, $\mathcal{K}_{\mathcal{F}\mathcal{T}}$, $\mathcal{K}_{\mathcal{F}}$, are the blocks of the stiffness matrix, $U_{\mathcal{T}}$ and $U_{\mathcal{F}}$ are the components of the vector of unknowns and $\mathbf{F}_{\mathcal{T}}$ is the cell source term (the face source term is null). A crucial observation is that both $\mathcal{K}_{\mathcal{T}}$ and $\mathcal{K}_{\mathcal{F}}$ are block diagonal. This important property will be exploited in Section 4 in the context of implicit and explicit time-stepping schemes. While the block-diagonal structure of $\mathcal{K}_{\mathcal{T}}$ is obvious, let us briefly motivate why $\mathcal{K}_{\mathcal{F}}$ is also block-diagonal. First, this is the case for all $F \in \mathcal{F}^{\text{OF}} \cup \mathcal{F}^{\text{OS}}$ since the stabilization bilinear forms are local to each interior face for both fluid and solid subdomains, with local diagonal blocks of size $\dim P^k(F)$ or $\dim \mathbf{P}^k(F)$, respectively. Furthermore, for all $F \in \mathcal{F}^\Gamma$, the couplings are also local to the face, but the diagonal block in $\mathcal{K}_{\mathcal{F}}$ is of larger size, namely $\dim P^k(F) + \dim \mathbf{P}^k(F)$.

4 Fully discrete schemes

The time discretization is based on Runge–Kutta (RK) schemes. Butcher tableaux are a classical way to define RK schemes by means of the coefficients $\{a_{ij}\}_{1 \leq i,j \leq s}$, $\{b_i\}_{1 \leq i \leq s}$, and $\{c_i\}_{1 \leq i \leq s}$, where $s \geq 1$ is the number of stages. For explicit RK schemes with s stages and order s (ERK(s)), the matrix $\{a_{ij}\}_{1 \leq i,j \leq s}$ is strictly lower-triangular. For singly diagonal implicit RK schemes with s stages and order $(s+1)$ (SDIRK($s, s+1$)), the matrix is lower-triangular with $a_{11} = \dots = a_{ss} := a_*$. The corresponding Butcher tableaux are as follows:

$$\begin{array}{c|cccc} c_1 & a_* & 0 & \cdots & 0 \\ c_2 & a_{21} & a_* & \ddots & 0 \\ \vdots & \vdots & \ddots & \ddots & \vdots \\ c_s & a_{s1} & \cdots & a_{s,s-1} & a_* \end{array} \quad \begin{array}{c|ccccc} c_1 & 0 & \cdots & \cdots & 0 \\ c_2 & a_{21} & 0 & \cdots & 0 \\ \vdots & \vdots & \ddots & \ddots & \vdots \\ c_s & a_{s1} & \cdots & a_{s,s-1} & 0 \end{array} \quad (4.1)$$

$$\begin{array}{c|cccc} & b_1 & \cdots & b_{s-1} & b_s \\ \hline & b_1 & \cdots & b_{s-1} & b_s \end{array}$$

To simplify the writing of SDIRK and ERK schemes, we define $a_{s+1,i} := b_i$ for all $i \in \{1, \dots, s\}$ and set $a_{s+1,s+1} := 0$.

We now detail the time discretization of (3.16) by SDIRK and ERK schemes. We show that an effective SDIRK implementation is obtained by the local elimination of the cell unknowns, whereas an effective ERK implementation is obtained by the local elimination of the face unknowns. The outcome of this elimination is illustrated in Figure 4. Let $(t^n)_{n \in \{0, \dots, N\}}$ with $t^0 = 0$ and $t^N = T_f$ be the discrete time nodes, and let $\Delta t^n := t^n - t^{n-1}$ be the time step. For simplicity, we consider that the time-step is constant and drop the superscript n .

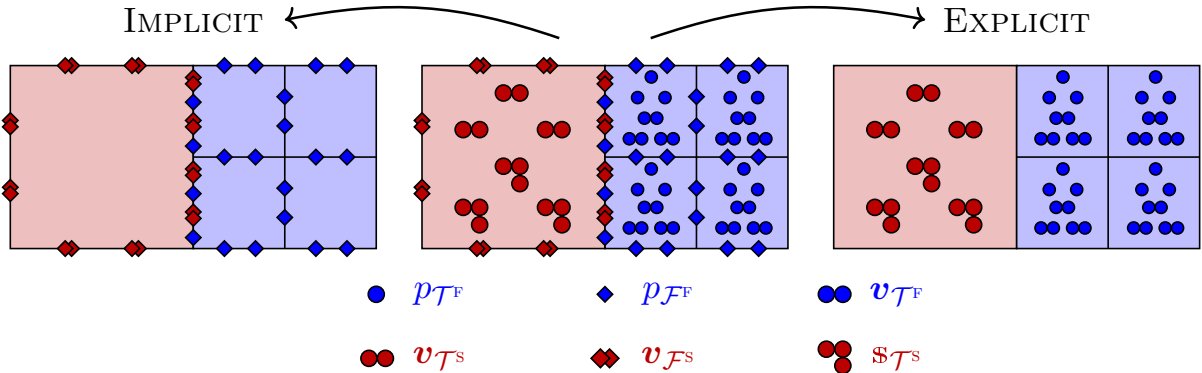


Fig. 4: Fully coupled unknowns after static condensation for SDIRK schemes (left) and for ERK schemes (right) for the lowest equal-order discretization ($k' = k = 1$).

We observe from Figure 4 that the number of cell dofs appears to be larger than the face dofs. Let us give a more quantitative estimate. Neglecting the number of boundary faces, and assuming that each cell has n faces (e.g., $n = 3$ for triangles and $n = 4$ for tetrahedra), the asymptotic ratio between the number of cells and the number of faces is $n \cdot \# \text{CELLS} \approx 2 \# \text{FACES}$. Under this assumption, Table 1 reports the expected percentage of dofs associated with faces for triangular and tetrahedral meshes, and for equal- and mixed-order HHO settings. A first observation is, as expected, that the proportion of face dofs decreases with the polynomial degree. A second observation is that, in the mixed-order case (used with implicit time schemes), the share of cell dofs is at least 75%. In this setting, static condensation — which eliminates the cell dofs — allows for a significant reduction in the size of the global linear system. In the equal-order case (used with explicit time schemes), the proportion of cell dofs is smaller but remains dominant (at least 67%). Here, the static condensation eliminates face dofs instead, which still reduces the system size, albeit less substantially. Altogether, we can conclude that the reduction in computational costs by static condensation is much more impactful when using implicit time schemes.

4.1 Singly Diagonal Implicit Runge-Kutta (SDIRK) schemes

Given $\mathbf{U}_{\mathcal{T}}^{n-1}$ from the previous time step or the initial condition, the time discretization of (3.16) by SDIRK($s, s + 1$) schemes is as follows: We solve sequentially for all $i \in \{1, \dots, s + 1\}$,

$$\begin{bmatrix} \mathcal{M}_{\mathcal{T}} & 0 \\ 0 & 0 \end{bmatrix} \begin{bmatrix} \mathbf{U}_{\mathcal{T}}^{n,i} \\ \mathbf{U}_{\mathcal{F}}^{n,i} \end{bmatrix} = \begin{bmatrix} \mathcal{M}_{\mathcal{T}} & 0 \\ 0 & 0 \end{bmatrix} \begin{bmatrix} \mathbf{U}_{\mathcal{T}}^{n-1} \\ \mathbf{U}_{\mathcal{F}}^{n-1} \end{bmatrix} + \Delta t \sum_{j=1}^i a_{ij} \left(\begin{bmatrix} \mathbf{F}_{\mathcal{T}}^{n-1+c_j} \\ 0 \end{bmatrix} - \begin{bmatrix} \mathcal{K}_{\mathcal{T}} & \mathcal{K}_{\mathcal{T}\mathcal{F}} \\ \mathcal{K}_{\mathcal{F}\mathcal{T}} & \mathcal{K}_{\mathcal{F}} \end{bmatrix} \begin{bmatrix} \mathbf{U}_{\mathcal{T}}^{n,j} \\ \mathbf{U}_{\mathcal{F}}^{n,j} \end{bmatrix} \right), \quad (4.2)$$

where $\mathbf{F}_{\mathcal{T}}^{n-1+c_j} := \mathbf{F}_{\mathcal{T}}(t_{n-1} + c_j \Delta t)$. Notice that the last stage ($i = s + 1$) only requires a mass matrix inversion. Finally, we set $\mathbf{U}_{\mathcal{T}}^{n+1} := \mathbf{U}_{\mathcal{T}}^{n,s+1}$. For all $i \in \{1, \dots, s\}$, each stage in (4.2) can be

		GENERAL k		$k = 1$	$k = 2$	$k = 3$
EQUAL-ORDER	2D	ACOUSTIC	$\frac{1}{k+3}$	25%	20%	17%
		ELASTIC	$\frac{6}{5k+16}$	29%	23%	19%
	3D	ACOUSTIC	$\frac{3}{2k+9}$	27%	23%	20%
		ELASTIC	$\frac{2}{k+5}$	33%	29%	25%
MIXED-ORDER	2D	ACOUSTIC	$\frac{3(k+1)}{3k^2+14k+13}$	20%	17%	15%
		ELASTIC	$\frac{6(k+1)}{5k^2+25k+24}$	22%	19%	17%
	3D	ACOUSTIC	$\frac{6(k+1)(k+2)}{4k^3+33k^2+77k+54}$	21%	19%	17%
		ELASTIC	$\frac{6(k+1)(k+2)}{3k^3+27k^2+66k+48}$	25%	23%	21%

Tab. 1: Percentage of face dofs for purely acoustic and elastic cases, in 2D and 3D, for equal- and mixed-order settings, for various polynomial degrees k .

rewritten as

$$\begin{bmatrix} \mathcal{M}_{\mathcal{T}} + a_* \Delta t \mathcal{K}_{\mathcal{T}} & a_* \Delta t \mathcal{K}_{\mathcal{T}\mathcal{F}} \\ a_* \Delta t \mathcal{K}_{\mathcal{F}\mathcal{T}} & a_* \Delta t \mathcal{K}_{\mathcal{F}} \end{bmatrix} \begin{bmatrix} \mathbf{U}_{\mathcal{T}}^{n,i} \\ \mathbf{U}_{\mathcal{F}}^{n,i} \end{bmatrix} = \begin{bmatrix} \mathbf{B}_{\mathcal{T}}^{n,i} \\ \mathbf{B}_{\mathcal{F}}^{n,i} \end{bmatrix}, \quad (4.3)$$

with

$$\begin{bmatrix} \mathbf{B}_{\mathcal{T}}^{n,i} \\ \mathbf{B}_{\mathcal{F}}^{n,i} \end{bmatrix} := \begin{bmatrix} \mathcal{M}_{\mathcal{T}} \mathbf{U}_{\mathcal{T}}^{n-1} + a_* \Delta t \mathcal{F}_{\mathcal{T}}^{n-1+c_i} + \Delta t \sum_{j=1}^{i-1} a_{ij} (\mathcal{F}_{\mathcal{T}}^{n-1+c_j} - \mathcal{K}_{\mathcal{T}} \mathbf{U}_{\mathcal{T}}^{n,j} - \mathcal{K}_{\mathcal{T}\mathcal{F}} \mathbf{U}_{\mathcal{F}}^{n,j}) \\ -\Delta t \sum_{j=1}^{i-1} a_{ij} (\mathcal{K}_{\mathcal{F}\mathcal{T}} \mathbf{U}_{\mathcal{T}}^{n,j} + \mathcal{K}_{\mathcal{F}} \mathbf{U}_{\mathcal{F}}^{n,j}) \end{bmatrix}. \quad (4.4)$$

A key observation is that the cell-cell submatrix in (4.3) (associated with all the fluid and solid cell unknowns) is block-diagonal. Hence, a static condensation procedure can be performed, leading to a global problem coupling only the face unknowns. This strategy enhances computational efficiency by eliminating locally all the cell unknowns. Therefore, (4.2) is solved by performing sequentially the following two solves:

$$a_* \Delta t (\mathcal{K}_{\mathcal{F}} - a_* \Delta t \mathcal{K}_{\mathcal{F}\mathcal{T}} (\mathcal{M}_{\mathcal{T}} + a_* \Delta t \mathcal{K}_{\mathcal{T}})^{-1} \mathcal{K}_{\mathcal{T}\mathcal{F}}) \mathbf{U}_{\mathcal{F}}^{n,i} = \mathbf{B}_{\mathcal{F}}^{n,i} - a_* \Delta t \mathcal{K}_{\mathcal{F}\mathcal{T}} (\mathcal{M}_{\mathcal{T}} + a_* \Delta t \mathcal{K}_{\mathcal{T}})^{-1} \mathbf{B}_{\mathcal{T}}^{n,i}, \quad (4.5a)$$

$$\mathbf{U}_{\mathcal{T}}^{n,i} = (\mathcal{M}_{\mathcal{T}} + a_* \Delta t \mathcal{K}_{\mathcal{T}})^{-1} (\mathbf{B}_{\mathcal{T}}^{n,i} - a_* \Delta t \mathcal{K}_{\mathcal{T}\mathcal{F}} \mathbf{U}_{\mathcal{F}}^{n,i}). \quad (4.5b)$$

Owing to the singly diagonal structure of the Butcher tableau, all the stages share the same system matrix allowing to re-use matrix factorizations. Moreover, for a constant time step, matrix factorizations can be re-used throughout the whole time integration. Notice also that the second step (4.5b) is local and embarrassingly parallel.

In this work, we employ s -stage Singly Diagonally Implicit Runge–Kutta (SDIRK) methods of order $(s+1)$, with $s \in \{2, 3\}$. The associated Butcher tableaux are reported in (4.6) where the

SDIRK(3, 4) scheme corresponds to the values $\nu := \frac{1}{\sqrt{3}} \cos(\frac{\pi}{18}) + \frac{1}{2}$ and $\xi := \frac{1}{6(2\nu-1)^2}$:

$$\begin{array}{c|cc} \frac{1}{4} & \frac{1}{4} & 0 \\ \hline \frac{3}{4} & \frac{1}{2} & \frac{1}{4} \\ \hline & \frac{1}{2} & \frac{1}{2} \end{array} \quad \begin{array}{c|ccc} \nu & \nu & 0 & 0 \\ \hline \frac{1}{2} & \frac{1}{2} - \nu & \nu & 0 \\ 1 - \nu & 2\nu & 1 - 4\nu & \nu \\ \hline & \xi & 1 - 2\xi & \xi \end{array} \quad (4.6)$$

4.2 Explicit Runge–Kutta (ERK) schemes

Given \mathbf{U}_T^{n-1} from the previous time step or the initial condition, the time discretization of (3.16) by ERK(s) schemes is as follows: We solve sequentially for all $i \in \{1, \dots, s+1\}$,

$$\begin{bmatrix} \mathcal{M}_T & 0 \\ 0 & 0 \end{bmatrix} \begin{bmatrix} \mathbf{U}_T^{n,i} \\ \mathbf{U}_{\mathcal{F}}^{n,i} \end{bmatrix} = \begin{bmatrix} \mathcal{M}_T & 0 \\ 0 & 0 \end{bmatrix} \begin{bmatrix} \mathbf{U}_T^{n-1} \\ \mathbf{U}_{\mathcal{F}}^{n-1} \end{bmatrix} + \Delta t \sum_{j=1}^{i-1} a_{ij} \left(\begin{bmatrix} \mathbf{F}_T^{n-1+c_j} \\ 0 \end{bmatrix} - \begin{bmatrix} \mathcal{K}_T & \mathcal{K}_{\mathcal{F}\mathcal{T}} \\ \mathcal{K}_{\mathcal{F}\mathcal{T}} & \mathcal{K}_{\mathcal{F}} \end{bmatrix} \begin{bmatrix} \mathbf{U}_T^{n,j} \\ \mathbf{U}_{\mathcal{F}}^{n,j} \end{bmatrix} \right), \quad (4.7)$$

recalling that $\mathbf{F}_T^{n-1+c_j} := \mathbf{F}_T(t_{n-1} + c_j \Delta t)$. Finally, we set $\mathbf{U}_T^{n+1} := \mathbf{U}_T^{n,s+1}$. This time, we exploit the fact that the face-face submatrix $\mathcal{K}_{\mathcal{F}}$ is block-diagonal and we eliminate locally all the face unknowns. Thus, we rewrite (4.7) only in terms of the cell unknowns (this procedure is called dG rewriting in the context of HDG methods). We first set $\mathbf{U}_T^{n,1} = \mathbf{U}_T^{n-1}$. Then, for all $i \in \{1, \dots, s+1\}$, we first solve:

$$\mathcal{K}_{\mathcal{F}} \mathbf{U}_{\mathcal{F}}^{n,i} = -\mathcal{K}_{\mathcal{F}\mathcal{T}} \mathbf{U}_T^{n,i}, \quad (4.8a)$$

followed by

$$\mathcal{M}_T \mathbf{U}_T^{n,i} = \mathcal{M}_T \mathbf{U}_T^{n-1} + \Delta t \sum_{j=1}^{i-1} a_{ij} \left(\mathbf{F}_T^{n-1+c_j} - (\mathcal{K}_T - \mathcal{K}_{\mathcal{F}\mathcal{T}} \mathcal{K}_{\mathcal{F}}^{-1} \mathcal{K}_{\mathcal{F}\mathcal{T}}) \mathbf{U}_T^{n,j} \right). \quad (4.8b)$$

We emphasize that both solves in (4.8) are block-diagonal.

In this work, we use s -stage Explicit Runge–Kutta (ERK) schemes of order s , with $s \in \{2, 3, 4\}$. The corresponding Butcher tableaux are reported in (4.9). We recall that ERK(s) schemes are subject to a CFL stability condition. This point is further discussed in Section 5.1 below.

$$\begin{array}{c|cc} 0 & 0 & 0 \\ \hline \frac{1}{2} & \frac{1}{2} & 0 \\ \hline & 0 & 1 \end{array} \quad \begin{array}{c|ccc} 0 & 0 & 0 & 0 \\ \hline \frac{1}{2} & \frac{1}{2} & 0 & 0 \\ \hline 1 & -1 & 2 & 0 \\ \hline & \frac{1}{6} & \frac{2}{3} & \frac{1}{6} \end{array} \quad \begin{array}{c|cccc} 0 & 0 & 0 & 0 & 0 \\ \hline \frac{1}{2} & \frac{1}{2} & 0 & 0 & 0 \\ \hline \frac{1}{2} & 0 & \frac{1}{2} & 0 & 0 \\ \hline 1 & 0 & 0 & 1 & 0 \\ \hline & \frac{1}{6} & \frac{1}{3} & \frac{1}{3} & \frac{1}{6} \end{array} \quad (4.9)$$

5 Numerical results

In this section, we present 2D numerical results obtained with the HHO discretization of the elasto-acoustic problem described above. Our goal is threefold. Our first goal is to analyze the CFL condition of the explicit schemes and to perform a computational efficiency study comparing explicit and implicit schemes, in order to identify the most effective time-stepping strategy. To this purpose, we consider manufactured solutions. Our second goal is to assess the accuracy of the method using a classical test case with a Ricker wavelet as the initial condition, comparing the numerical results to a semi-analytical solution. Moreover, we provide a further comparison

between explicit and implicit schemes using this second test case. Our third goal is to showcase the geometric flexibility of the method. To this purpose, we consider a geophysical application involving the propagation of a seismic wavefield through complex media.

Recall that, for explicit time-stepping, we use an equal-order HHO discretization with $O(1)$ Least-Squares stabilization whereas, for implicit time-stepping, we use a mixed-order HHO discretization with Lehrenfeld-Schöberl $O(\frac{1}{h})$ -stabilization. To solve the resulting linear systems, both a direct LU solver and an iterative Biconjugate Gradient (BiCG) solver preconditioned by an incomplete LU (ILU) factorization are used. The former is considered so as to enable a fair comparison with the explicit schemes.

The implementation is carried out in the open-source software `disk++`, available at <https://github.com/wareHHOuse/diskpp>, and further detailed in [12].

5.1 CFL and efficiency study on a sinusoidal test case

To define the discretization level we introduce two computational parameters: the spatial refinement level ℓ , so that $h = 2^{-\ell}$, and the time refinement level n , so that $\Delta t = 0.1 \times 2^{-n}$. We consider three types of meshes: Cartesian, simplicial and polygonal. Some examples are shown in Figure 5 for $\ell = 2$, with the solid subdomain mesh on the left side in red, and the fluid subdomain mesh on the right side in blue.

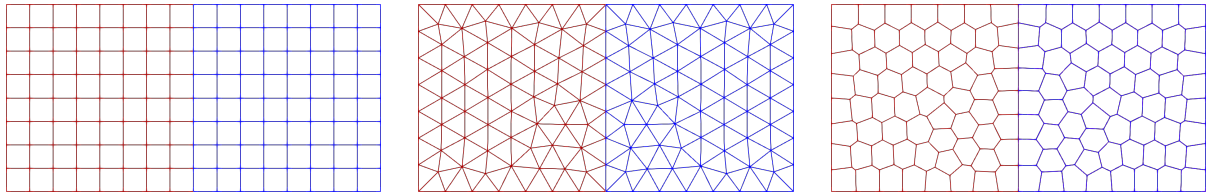


Fig. 5: Cartesian, simplicial, and polygonal meshes for $\ell = 2$.

Test case setting. The fluid and solid media have the same density and similar wave speeds. Specifically, we consider a simulation time $T_f := 1$ and

- $\Omega^F := (0, 1) \times (0, 1)$, with density $\rho^F := 1$, compressibility modulus $\kappa := 1$, so that the velocity of the pressure waves is $c_p^F = 1$;
- $\Omega^S := (-1, 0) \times (0, 1)$, with density $\rho^S := 1$, and Lamé parameters so that $c_p^S := \sqrt{3}$ and $c_s = 1$.

The sinusoidal solution is expressed in terms of the potential u (acoustic) and the displacement $\mathbf{u} := (u_x, u_y)$ (elastic) so that

$$p := \partial_t u, \quad \mathbf{m} := \nabla u, \quad \text{in } \Omega^F, \quad (5.1a)$$

$$\mathbf{v} := \partial_t \mathbf{u}, \quad \mathbb{C}^{-1} \mathbf{s} := \nabla_{\text{sym}} \mathbf{u}, \quad \text{in } \Omega^S. \quad (5.1b)$$

If not specified, the source terms, the (non)homogeneous Dirichlet boundary conditions, and the initial conditions are defined according to

$$u(t, x, y) := x^2 \sin(\omega \pi x) \sin(\omega \pi y) \sin(\theta \pi t), \quad (5.2a)$$

$$u_x(t, x, y) := u_y(t, x, y) = x^2 \cos(\omega \frac{\pi}{2} x) \sin(\omega \pi y) \cos(\theta \pi t), \quad (5.2b)$$

where ω and θ are the spatial and temporal frequencies, respectively. We consider two main configurations: a dominant spatial evolution with $\omega := 5$ and $\theta := \sqrt{2}$ and a dominant temporal evolution with $\omega := 1$ and $\theta := 10$.

Stability study of explicit time schemes. We first study the stability of ERK(s) schemes with $s \in \{2, 3, 4\}$. We consider additional weighting parameters, η^F and η^S , which scale the stabilization bilinear forms appearing on the right-hand sides of (3.10). The stability condition for the ERK(s) schemes can be written in the following form,

$$c_{\sharp} \frac{\Delta t}{h} \leq \text{CFL}^*(s, k, \eta^F, \eta^S), \quad (5.3)$$

where CFL^* denotes the critical value for stability and c_{\sharp} is the largest velocity in the domain. To determine the value of CFL^* , we use an empirical procedure based on energy conservation. To this purpose, we slightly modify the test case so that the energy of the system remains constant. Specifically, we consider the functions in (5.2) only to prescribe the initial condition, take homogeneous Dirichlet boundary conditions and impose null source terms. Stability is assessed based on the relative energy increase, limited to $\varepsilon := 5\%$ of the initial or previous time-step energy. At the time step t^n , the energy is evaluated as

$$E^n := \frac{1}{2} \|\mathbf{m}\tau(t^n)\|_{L^2(\rho^F; \Omega^F)}^2 + \frac{1}{2} \|p\tau(t^n)\|_{L^2(\frac{1}{\kappa}; \Omega^F)}^2 + \frac{1}{2} \|\mathbf{v}\tau(t^n)\|_{L^2(\rho^S; \Omega^S)}^2 + \frac{1}{2} \|\mathbf{s}\tau(t^n)\|_{\mathbb{L}^2(\mathbb{C}^{-1}; \Omega^S)}^2. \quad (5.4)$$

The value of CFL^* is determined by reducing iteratively the total number of time steps by $\delta := 1\%$ after each stable simulation. The value of CFL^* is then identified by bracketing the transition between stability and instability. The procedure is summarized in Algorithm 1.

Algorithm 1 Bounding of the CFL Stability Limit

```

1: while simulation is stable do
2:   for  $n = 1$  to  $N$  do
3:     Compute energy  $E_n$ 
4:     Compute relative energy increase  $\Delta E := \max_n \left( \frac{|E_n - E_0|}{E_0}, \frac{|E_n - E_{n-1}|}{E_{n-1}} \right)$ 
5:     if  $\Delta E > \varepsilon$  then
6:       Flag  $N$  as the first unstable time step
7:       Break
8:     end if
9:   end for
10:  Flag  $N$  as the last stable time step
11:  Decrease  $N$  by  $\delta N$ 
12: end while

```

In Figure 6, we first analyze the stability of the pure acoustic and elastic problems to determine the optimal values of η^F and η^S in each subdomain, *i.e.* the values that maximize CFL^* . We obtain $\eta_*^F = 0.8$ and $\eta_*^S = 1.5$. These values are retained in the rest of the paper. We also notice that the stability coefficient CFL^* behaves as $\min(\eta + c_1, \frac{1}{\eta} + c_2)$ for suitable constants c_1 and c_2 , consistently with the observations reported in [45] for the spectral radius of the stiffness matrix.

In Table 2, we report the CFL^* values determined using Algorithm 1. These tables also provide the ratios of the CFL^* coefficients between the different number of stages of the ERK(s) schemes and the different polynomial orders, respectively. It can be observed that these ratios slightly increase with s , showing that increasing the number of stages improves stability. Moreover, as expected, CFL^* decreases with the polynomial degree, essentially as k^{-1} . Finally, in Table 3, we analyze the impact of the mesh geometry on the value of CFL^* . This value is only mildly sensitive to the mesh geometry, although meshes with higher face counts seem to slightly enhance the scheme stability.

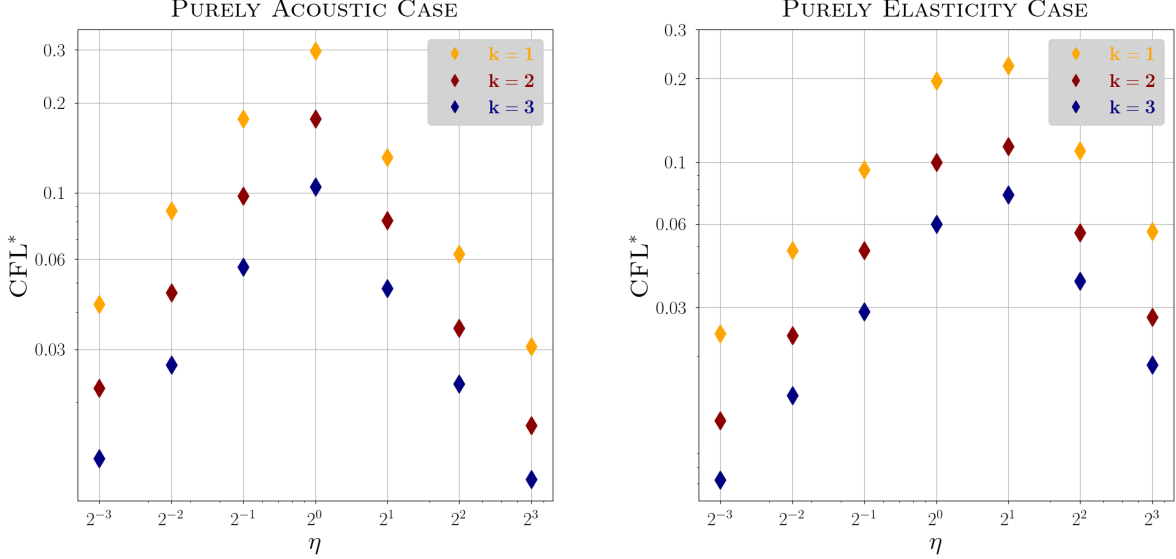


Fig. 6: CFL* in the equal-order setting for the pure acoustic and elastic cases for $k \in \{1, 2, 3\}$.

	$k = 1$			$k = 2$			$k = 3$		
	$s = 2$	$s = 3$	$s = 4$	$s = 2$	$s = 3$	$s = 4$	$s = 2$	$s = 3$	$s = 4$
CFL*	0.205	0.253	0.282	0.099	0.123	0.138	0.063	0.079	0.087
RATIO WRT s	1	1.23	1.38	1	1.24	1.39	1	1.25	1.38
RATIO WRT k	1	1	1	0.48	0.49	0.49	0.31	0.31	0.31

Tab. 2: CFL* coefficient (and ratios thereof) for ERK(s), $s \in \{2, 3, 4\}$ and $k \in \{1, 2, 3\}$.

MESHES	$s = 2$			$s = 3$			$s = 4$			
	\triangle	\square	\diamond	\triangle	\square	\diamond	\triangle	\square	\diamond	
$k = 1$	CFL*	0.191	0.205	0.264	0.238	0.253	0.329	0.265	0.282	0.363
	RATIO	1	1.07	1.38	1	1.06	1.38	1	1.06	1.37
$k = 2$	CFL*	0.106	0.099	0.136	0.133	0.123	0.170	0.147	0.138	0.188
	RATIO	1	0.93	1.28	1	0.92	1.28	1	0.94	1.28
$k = 3$	CFL*	0.072	0.063	0.082	0.090	0.079	0.102	0.100	0.087	0.115
	RATIO	1	0.88	1.13	1	0.88	1.13	1	0.87	1.15

Tab. 3: CFL* coefficient (and ratios thereof) for ERK(s), $s \in \{2, 3, 4\}$ and $k \in \{1, 2, 3\}$.

Efficiency study. We now assess the efficiency of the explicit and implicit schemes using the analytical solution (5.2). Accuracy is quantified by computing the error in the L^2 -norm of the dG variables at the final time step over the computational domain. The efficiency of the various schemes is compared in terms of error versus CPU time. For a fair comparison, implicit schemes employ an iterative solver with a tolerance defined as $TOL_\ell := 2^{-\ell(k+1)}TOL_0$ so that at each level of space refinement, the convergence criterion for the iterative solver is decreased appropriately. Moreover, for both implicit and explicit schemes of order s , the time steps are defined as $\Delta t_\ell := 2^{-\ell \frac{k+1}{s+1}} \Delta t_0$ so as to ensure that, at each level of space refinement, the space and time discretization errors remain balanced. The reference parameters TOL_0 and Δt_0 are determined empirically. Specifically, we compute the error associated with various time step values and observe a stagnation of the total error once the time discretization error becomes negligible compared to the spatial discretization error. We then define Δt_0 as the largest time step for which this stagnation is observed. The

reference tolerance TOL_0 is selected slightly smaller than the spatial discretization error to ensure that the iterative solver does not dominate the total error. This procedure, which is only considered for $\ell = 0$, yields an optimized implicit time step for solving the problem. The time step for explicit schemes is instead dictated by the CFL condition (5.3) for all $\ell \geq 0$.

In Figure 7 and Figure 8, we first consider the test case in which the spatial discretization error dominates. In Figure 7, our objective is to compare explicit schemes on the one hand, and implicit schemes on the other hand. The first observation, valid for both explicit and implicit schemes, is that increasing the polynomial degree significantly improves efficiency. The second observation is that, in the regime where the spatial error dominates, all the explicit schemes exhibit similar efficiency, and the same holds for implicit schemes. Nevertheless, ERK(2) and SDIRK(3,4) appear to be slightly more efficient than the other schemes within their respective category. In Figure 8, the left panel compares the efficiency of ERK(2) and SDIRK(3,4) schemes. We observe that the implicit scheme is more efficient than the explicit one. This gain is due to the larger time steps allowed by the implicit scheme and the elimination of cell unknowns by static condensation, which compensates for the additional cost of solving the linear system. In the right panel, we evaluate the efficiency of ERK(4) on meshes composed of different cell geometries: simplices, polygons, and squares. We observe that, overall, the efficiency remains similar across the three mesh types. However, at low polynomial orders, polygonal meshes appear to be slightly more efficient, as their more favorable CFL condition allows for somewhat larger time steps. Conversely, at higher orders, the large number of faces in polygonal meshes becomes a drawback. Indeed, the better CFL condition no longer offsets the additional computational cost due to the handling of extra faces. Hence, while the overall efficiency remains comparable, we can conclude that polygonal meshes are preferable at low order, whereas at higher order, it is advantageous to favor cell geometries with fewer faces, such as simplices.

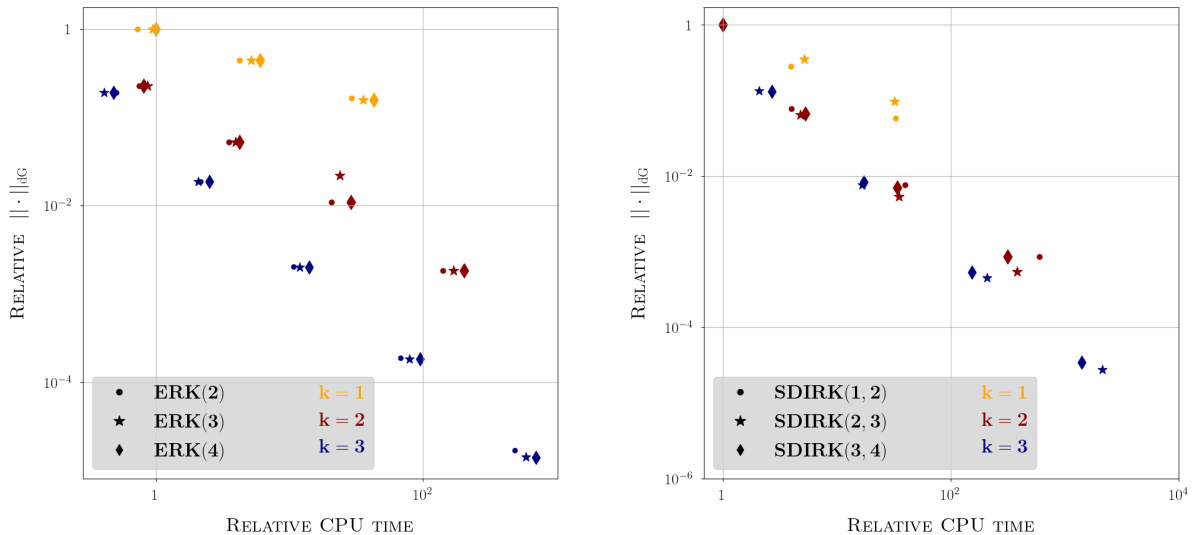


Fig. 7: Test case with dominant spatial error. **Left panel:** Efficiency comparison for $ERK(s)$ for $s \in \{2, 3, 4\}$. **Right panel:** Efficiency for $SDIRK(s, s + 1)$ for $s \in \{1, 2, 3\}$.

In Figure 9, we now consider the test case where the time error is dominant. In this setting, the time steps used for the implicit schemes are smaller than the stability limit enforced by (5.3). Therefore, there is no advantage in using implicit schemes. Regarding the cell geometry, since the stability constraint is no longer the limiting factor, reducing the number of faces is the most effective approach, regardless of the approximation order.

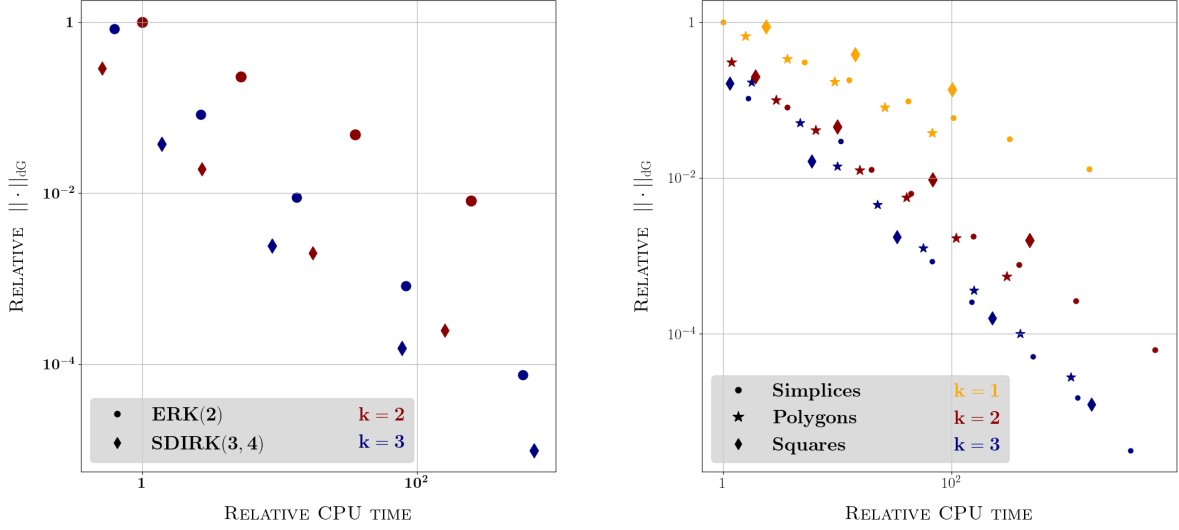


Fig. 8: Test case with dominant spatial error. **Left panel:** Efficiency comparison for ERK(2) and SDIRK(3,4). **Right panel:** Efficiency comparison for ERK(4) on meshes composed of different cell geometries.

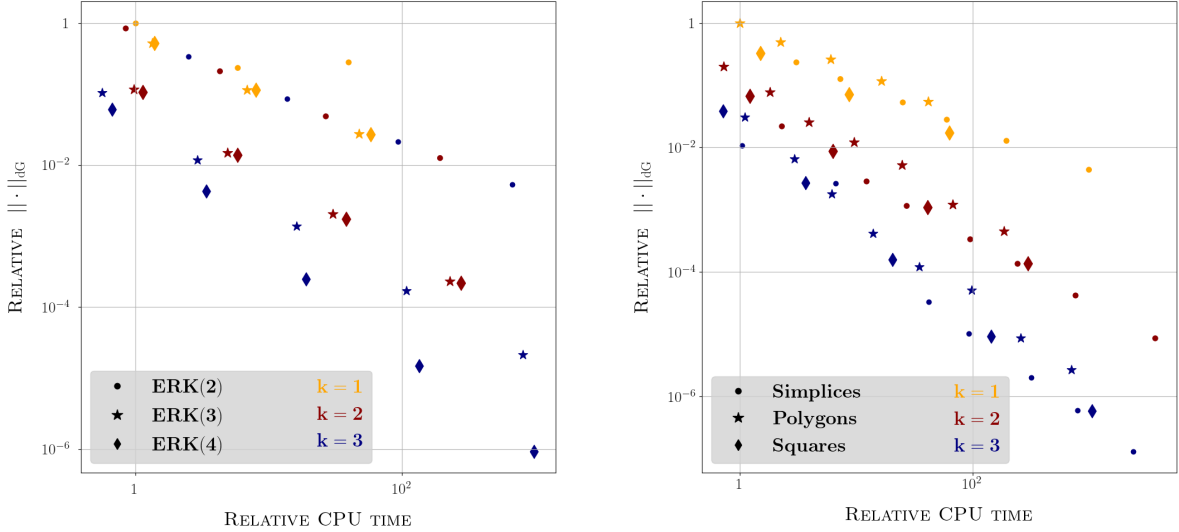


Fig. 9: Test case with dominant time error. **Left panel:** Efficiency comparison for ERK(s) for $s \in \{2, 3, 4\}$. **Right panel:** Efficiency comparison for ERK(4) on meshes composed of different cell geometries.

5.2 Accuracy study and efficiency on a Ricker wavelet

Here, we investigate the accuracy of the proposed method to simulate the propagation of an elasto-acoustic wave through a bilayered, stratified medium. Referring to Figure 10, let H denote the height of the whole domain, H^F and H^S the height of the fluid and solid subdomain respectively, and L the width of both subdomains. We define $\Omega^F := (0, L) \times (0, H^F)$ for the fluid subdomain and $\Omega^S := (0, L) \times (-H^S, 0)$ for the solid subdomain. Homogeneous Dirichlet boundary conditions are applied, the source terms are set to zero, and the perturbation to quiescence is due to the initial velocity field that is a Ricker wavelet centered at the point $(x_c, y_c) \in \Omega^F$ (indicated in purple in

Figure 10), expressed as

$$\mathbf{m}_0(x, y) := \theta \exp\left(-\pi^2 \frac{r^2}{\lambda^2}\right) (x - x_c, y - y_c)^\dagger, \quad (5.5)$$

where $\theta := 1 \text{ [Hz]}$, $\lambda := \frac{c_F}{f_c} \text{ [m]}$ with $f_c := 10 \text{ [Hz]}$, and $r^2 := (x - x_c)^2 + (y - y_c)^2$.

Three virtual sensors record the properties of the propagating elasto-acoustic wavefield: \mathcal{S}^F , \mathcal{S}^S and \mathcal{S}^I , located in the fluid subdomain, in the solid subdomain and at the interface, respectively. The acoustic sensor \mathcal{S}^F records the acoustic pressure $p_{\mathcal{T}^F}$ and the fluid velocity $\mathbf{m}_{\mathcal{T}^F}$, whereas the elastic sensor \mathcal{S}^S records the elastic velocity $\mathbf{v}_{\mathcal{T}^S}$ and the stress tensor $\mathbf{s}_{\mathcal{T}^S}$. The sensor located at the interface records the four quantities $p_{\mathcal{F}^F}$, $\mathbf{m}_{\mathcal{F}^F}$, $\mathbf{v}_{\mathcal{F}^S}$ and $\mathbf{s}_{\mathcal{F}^S}$.

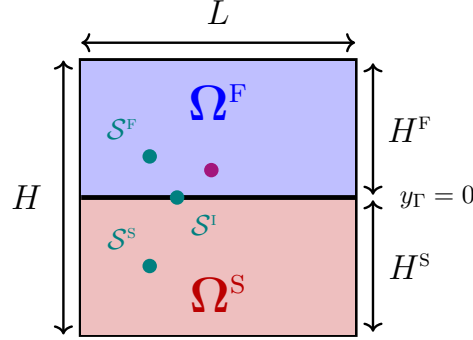


Fig. 10: General setting for the accuracy tests with a Ricker wavelet as an initial condition. Turquoise dots indicate the position of the three sensors and the magenta dot indicates the localization of the center of the initial source.

5.2.1 Academic material properties

We first consider an academic case in which the acoustic and elastic media exhibit identical densities and propagate the acoustic waves and the elastic S-waves at the same velocity as compressional acoustic waves, *i.e.*,

$$\rho^F := \rho^S := 1, \quad c_p^S := \sqrt{3}, \quad c_p^F := c_s^S := 1. \quad (5.6)$$

Concerning the geometry, we set $L := H := 1 \text{ [m]}$, $H^F := H^S := 0.5 \text{ [m]}$, and the pulse is located at $x_c := 0 \text{ [m]}$, $y_c := 0.125 \text{ [m]}$ in the fluid subdomain. The simulation time is set to $T_f := 1 \text{ [s]}$.

As observed below equations (2.6)-(2.7), the coupling conditions on Γ are weakly imposed. Here, we take a closer look at what happens at the interface so as to illustrate numerically the convergence results established in [45]. To this purpose, we use the sensor $\mathcal{S}^I := (-0.3, 0) \text{ [m]}$ and we set, for all $t \in \overline{J}$,

$$\Delta_{\text{KIN}}(t, \mathcal{S}^I) := |(\mathbf{v}_{\mathcal{F}^S}(t, \mathcal{S}^I) - \mathbf{m}_{\mathcal{T}^F}(t, \mathcal{S}^I)) \cdot \mathbf{n}_\Gamma|, \quad (5.7a)$$

$$\Delta_{\text{DYN}}(t, \mathcal{S}^I) := \|p_{\mathcal{F}^F}(t, \mathcal{S}^I) \mathbf{n}_\Gamma - \mathbf{s}_{\mathcal{T}^S}(t, \mathcal{S}^I) \cdot \mathbf{n}_\Gamma\|, \quad (5.7b)$$

The numerical results are obtained using SDIRK(3, 4) and the time step is set to $\Delta t = 0.1 \times 2^{-8}$ (this value is small enough so that space discretization errors dominate). Figure 11 reports the evolution at the discrete time nodes of the errors defined in (5.7), for various mesh refinement levels ℓ . The left column shows the kinematic errors (5.7a), whereas the right column shows the dynamic errors (5.7b). The top row corresponds to the polynomial degree $k = 1$ and the bottom row to $k = 3$. As expected, the numerical error on the pointwise satisfaction of the coupling conditions decreases significantly when increasing the mesh refinement and/or the polynomial degree

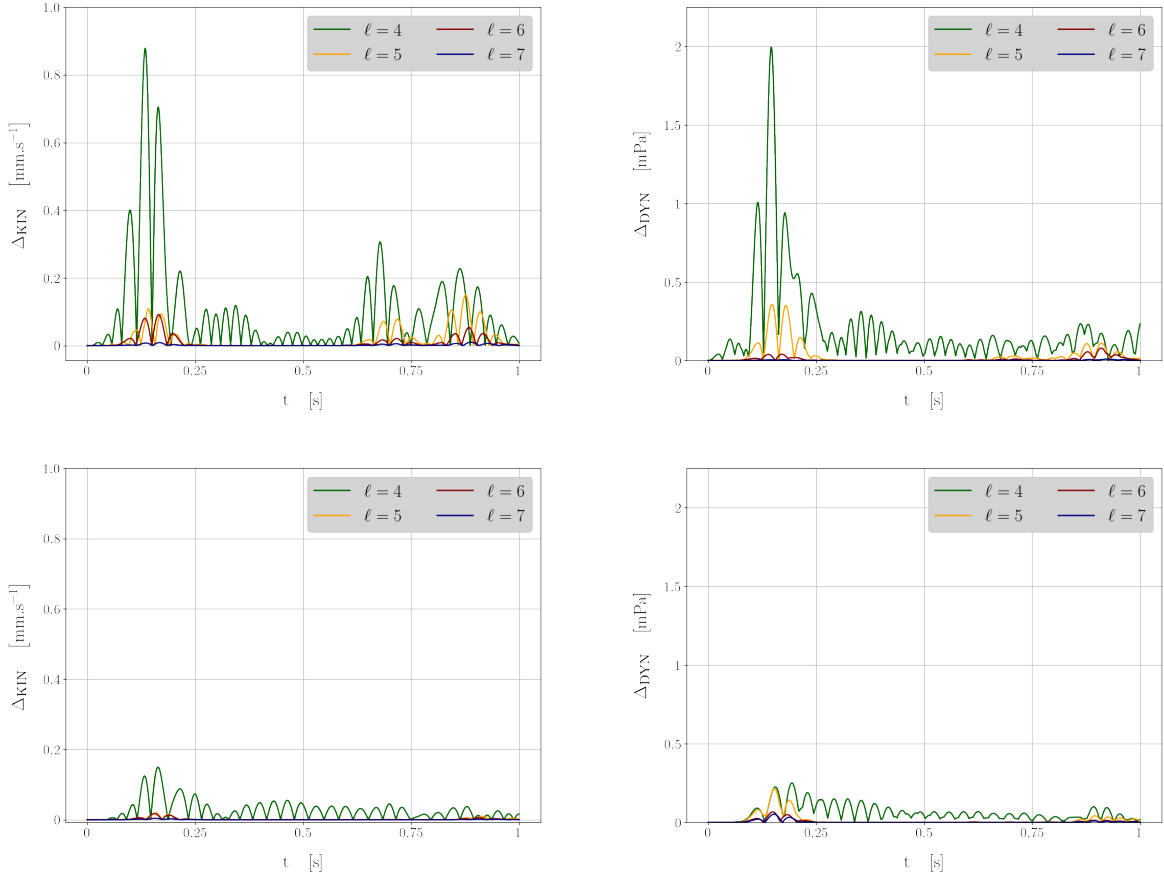


Fig. 11: Errors on the coupling conditions as a function of the time predicted by SDIRK(3,4) for $k = 1$ (top row) and $k = 3$ (bottom row). **Left:** Kinematic errors (see (5.7a)). **Right:** Dynamic errors (see (5.7b)).

5.2.2 Realistic (strongly contrasted) material properties

We now consider a test case with a strong contrast of material properties, specifically focusing on hard rock (granite) overlaid by a water layer with the following material properties:

$$\begin{aligned} \rho^F &:= 1025 \text{ kg.m}^{-3}, & c_p^F &:= 1500 \text{ m.s}^{-1}, \\ \rho^S &:= 2690 \text{ kg.m}^{-3}, & c_p^S &:= 6000 \text{ m.s}^{-1}, & c_s^S &:= 3000 \text{ m.s}^{-1}. \end{aligned} \quad (5.8)$$

The geometric setup is now $L := 7.5$ [km], $H := 5.25$ [km], $H^F := 1.5$ [km] and $H^S := 3.75$ [km], and the pulse is located at $x_c := 0$ [km], $y_c := 0.1$ [km] in the fluid subdomain. The simulation time is set to $T_f := 0.625$ [s]. The mesh is composed of quadrangular elements with size of $h_x = 23.3$ [m] and $h_y = 16.3$ [m].

The results are obtained using SDIRK(3,4) and the time step is set to $\Delta t = 0.1 \times 2^{-6}$. A semi-analytical reference solution, valid until reflections occur at the domain boundaries, is computed using the open source software Gar6more (<https://gitlab.inria.fr/jdiaz/gar6more2d>). Figure 12 displays the particularly rich structure of the pressure field in the fluid subdomain and of the Euclidian norm of the velocity field in the solid subdomain, both at final time. We observe the presence of conical and interface (Rayleigh, Scholte) waves, whose accurate capture is commonly used to assess the accuracy of a numerical method.

In Table 4 and Figure 13, we evaluate the accuracy of the numerical predictions at the three sensors located at $\mathcal{S}^F := (-2.3, 0.1)$ [km], $\mathcal{S}^S := (-2.3, -0.2)$ [km] and $\mathcal{S}^I := (-1.3, 0)$ [km]. The sensors \mathcal{S}^F and \mathcal{S}^S located within the two subdomains are positioned so as to capture only the conical

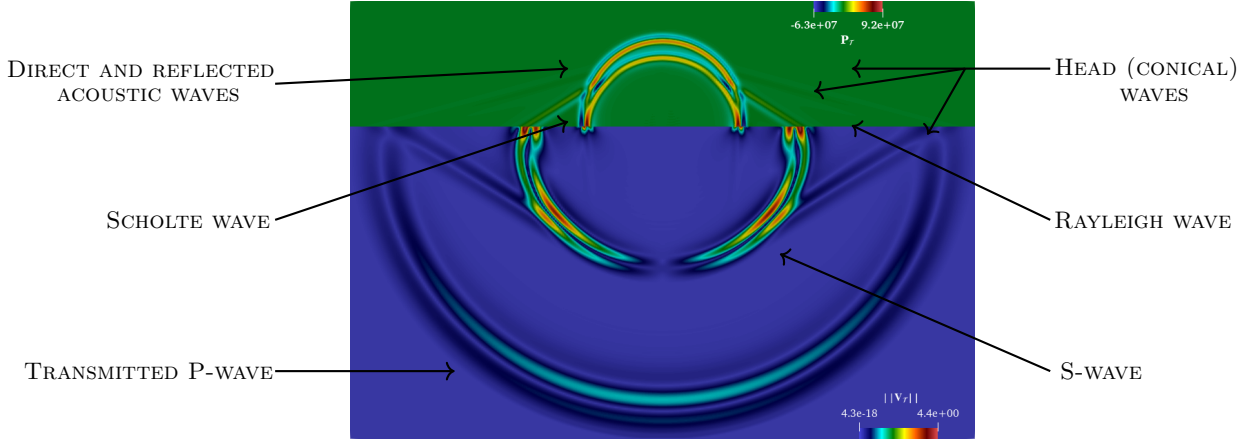


Fig. 12: Spatial distribution of the acoustic pressure (upper side) and the elastic velocity norm (lower side) at $t = 0.625$ [s].

waves, whereas the sensor \mathcal{S}^I located at the interface also captures the main phases. We compare ERK(4) and SDIRK(3, 4) and to avoid the proliferation of results, we focus on the polynomial degrees $k \in \{2, 3\}$ in Table 4 and $k \in \{1, 3\}$ in Figure 13. CPU times and relative errors with respect to the reference solution, measured at the sensors \mathcal{S}^F and \mathcal{S}^S , are reported in Table 4. The relative error is defined as

$$\text{ERR} := \frac{\|p_{\mathcal{T}^F}(t, \mathcal{S}^F) - p_{\text{REF}}(t, \mathcal{S}^F)\|_{\ell^2(J)}}{\|p_{\text{REF}}(t, \mathcal{S}^F)\|_{\ell^2(J)}} + \frac{\|\mathbf{v}_{\mathcal{T}^S}(t, \mathcal{S}^S) - \mathbf{v}_{\text{REF}}(t, \mathcal{S}^S)\|_{\ell^2(J)}}{\|\mathbf{v}_{\text{REF}}(t, \mathcal{S}^S)\|_{\ell^2(J)}}. \quad (5.9)$$

Notice that all the methods compared in Table 4 lead to comparable errors, so that the CPU comparison is meaningful concerning their efficiency. For the explicit scheme, we consider time steps just slightly below the stability limit. Instead, for the implicit scheme, we can consider larger time steps. In each case, the time step Δt is reported in nondimensional form as $\tilde{\Delta t} := c_p^s \frac{\Delta t}{h}$, where c_p^s is defined in (5.8) and is the largest velocity in the domain. We observe in Table 4 that the difference is significant between implicit and explicit time schemes. In particular, for $k = 3$, the CPU ratio reaches nearly 7, since much smaller time steps are required for explicit schemes. This negatively impacts the overall CPU time, confirming as in the previous section the higher efficiency reached by implicit schemes. Referring now to Figure 13, we notice that, for $k = 1$, the spatial resolution is insufficient to accurately capture the solution, whereas, for $k = 3$, accurate solutions are captured when $\tilde{\Delta t} \leq 0.414$.

SCHEMES	SOLVER	CFL*	$\tilde{\Delta t}$	RATIO	CPU [s]	RATIO	ERR	
SDIRK(3, 4)	$k = 2$ $k = 3$	direct	n/a	0.414	6.90	1125	1	3.15e-02
				0.414	6.90	2284	2.03	2.52e-02
SDIRK(3, 4)	$k = 2$ $k = 3$	iterative	n/a	0.414	6.90	2228	1.98	3.91e-02
				0.414	6.90	4216	3.75	3.11e-02
ERK(4)	$k = 2$ $k = 3$	n/a	0.138 0.087	0.095 0.060	1.36 1	1533 5664	1.27 5.03	2.01e-2 1.90e-2

Tab. 4: Times step $\tilde{\Delta t}$ (normalized as CFL*), CPU times and errors (see (5.9)) for ERK(s) for $s \in \{2, 3, 4\}$ and $k \in \{2, 3\}$.

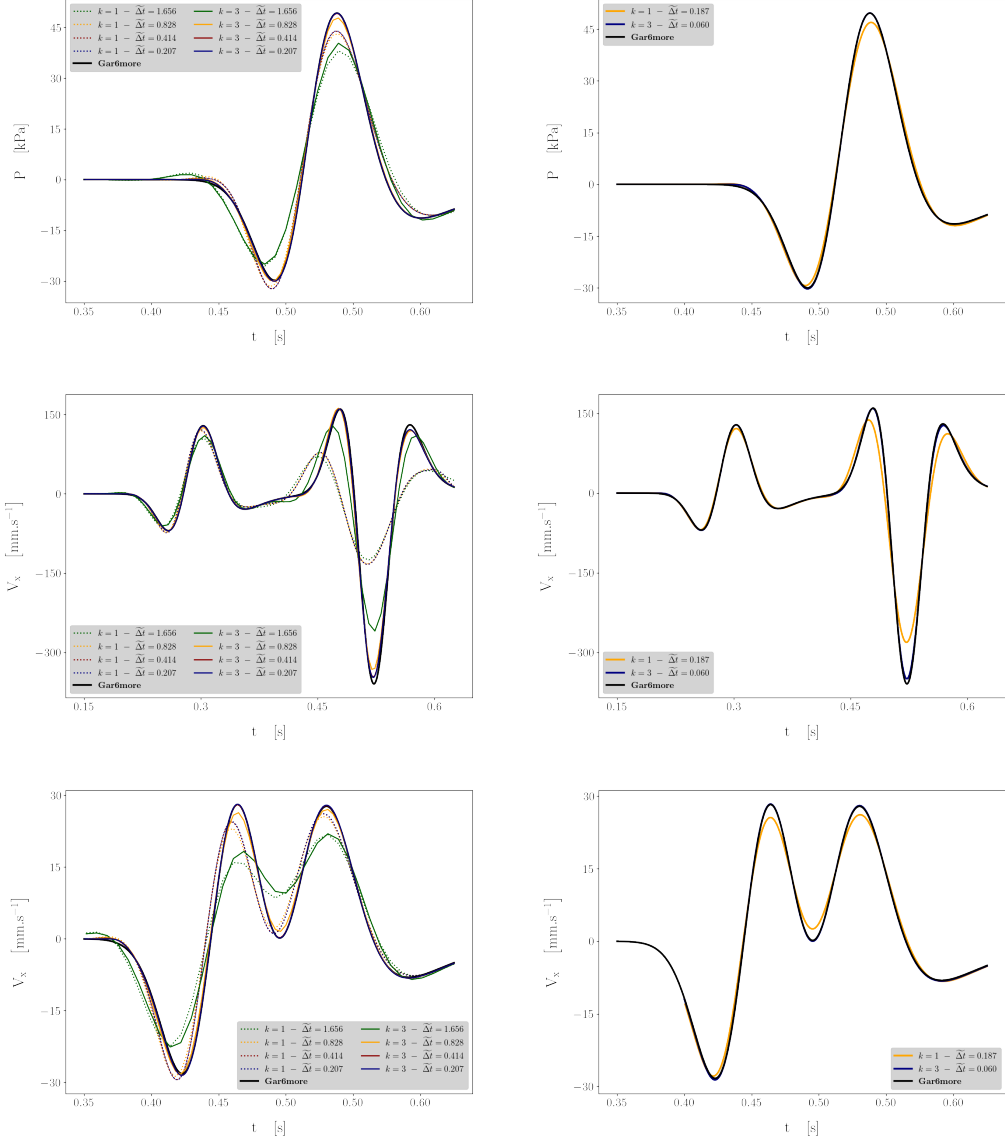


Fig. 13: Spatial distribution of the acoustic pressure at \mathcal{S}^F (top row), x -component of the velocity at \mathcal{S}^I (center row) and \mathcal{S}^S (bottom row) at times $t \in [0, 0.625]$ [s]. **Left column:** SDIRK(3,4), $k \in \{1, 3\}$, and $\Delta t \in \{0.402, 0.805, 1.609, 3.219\}$. **Right column:** ERK(4), $k \in \{1, 3\}$ and $\Delta t = \{0.117, 0.363\}$ (recall that $CFL^* = 0.087$ for $k = 3$).

5.3 Geometric flexibility of HHO: a realistic simulation

Finally, we present a realistic test case of seismoacoustics coupling that is relevant in some geophysical applications. Namely, we are interested in the propagation of seismic waves that can be trapped in a sedimentary basin embedded in a hard rock, or bedrock, and such that large part of the energy can leak into the atmosphere. This phenomenon seems to have already been observed in [32, 5], and may be important for the monitoring of natural hazards or anthropogenic activities in areas where seismic arrays are sparse.

We restrict ourselves to a 2D simulation, because the high-performance computing tools for a realistic 3D simulation are not yet available in the present implementation of `disk++`. This study is thus to be considered as a proof-of-concept to showcase the benefits of using HHO methods through an ease in meshing procedures (polytopal flexibility). First, we illustrate that there is no need to

restrict the spatial discretization to a unique cell geometry. If this may not be that relevant in 2D (where a complete discretization with quadrangles is possible), it is clearly a nontrivial issue in 3D realistic situations [21, 9]. Second, we show that HHO allows one to perform straightforwardly simulations using a nonconforming mesh (that is, with hanging nodes).

5.3.1 Test case setting

The geological setting shown in the left panel of Figure 14 is rather simplistic, especially concerning the spatial dimensions (less than 10 km in each direction, namely the domain extends from -4 [km] to $+4$ [km] laterally, and from -6 [km] to 1.4 [km] vertically, with a solid-fluid boundary located around a height of $+1.1$ [km]), whereas interactions of the seismic wavefield with the sedimentary basin-atmosphere can happen several tens of kilometers away from the source [5]. Here, the source term is located under a small mountain (where coupling with the atmosphere is expected, see [11]), and a sedimentary basin is located 1 km away. The seismic motion is introduced as an initial condition in velocity, whose spatial distribution is that of a Ricker wavelet (as in (5.5)) with a central frequency of $f_c = 4$ Hz. The center of the Ricker wavelet is located at $(0.563, 0.233)$ [km] (see Figure 14). We consider a simulation time $T_f = 1.5$ [s], and material properties are reported in the right panel of Figure 14.

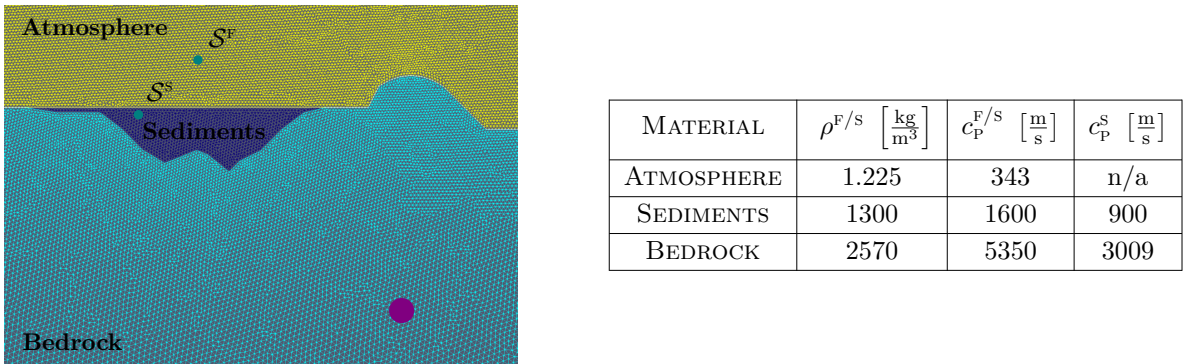


Fig. 14: **Left panel:** Slightly zoomed-in view of the mesh (with triangles) of the computational domain: a bedrock (such as granite, in turquoise) embeds a sedimentary basin (in dark blue); both are overlaid by a homogeneous atmosphere (in yellow). Sensors (turquoise dots): A barometric sensor S^F is positioned in the atmosphere and a seismometer S^S is positioned in the sedimentary basin. The center of the Ricker wavelet is indicated by a purple point. **Right panel:** Material properties.

Our goal is to discretize the geometry with a classical meshing software (here, `gmsh`), without having to extensively tune the meshing process. Three meshes have therefore been generated: the canonical mesh delivered by *gmsh* with only simplices (Figure 14, left panel); a second one with quadrangles only; and the last one, a hybrid mesh with both cell geometries (Figure 15, left panel). This latter hybrid mesh illustrates a common situation where, due to geometric complexity, it becomes difficult for the meshing software to maintain a unique geometrical shape for the mesh cells. As a result, undesired element types—typically simplices—are introduced locally within a mesh that was intended to be uniformly shaped. Dealing with this issue typically requires manually modifying the mesh to make it purely quadrangular, a process that can be cumbersome and that frequently results in elements with poor Jacobian conditioning. Moreover, from a coarse mesh, we also generate a nonconforming mesh with hanging nodes, following a one-step refinement in the atmosphere and in the basin (Figure 15, right panel). If both mixed and nonconforming meshes have already been used in other contexts [31], we underline that these can be naturally dealt with using HHO by leveraging its polytopal flexibility, without any specific extra procedure.

All the conforming meshes are generated in order for the acoustic waves and the associated interface waves to be sufficiently sampled in space, so as to suffer from minimal grid dispersion. This corresponds to a length scale of around 14 [m] along the Earth-atmosphere interface. The nonconforming mesh is generated starting from a characteristic size for the edge length of 28 [m], and then refining in the atmosphere and the sedimentary basin only. The number of cells is 185 923 for the triangular mesh, 94 019 for the quadrangular mesh, 93 490 for the hybrid mesh, and 84 204 for the nonconforming mesh.

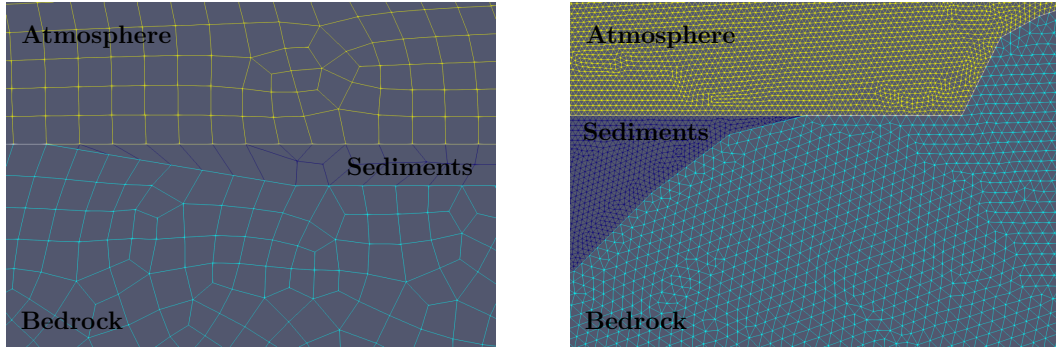


Fig. 15: **Left panel:** Hybrid mesh generated using `gmsh`: Most of the cells are quadrangles (more than 99%), but with remaining triangles in some parts of the domain. **Right panel:** Nonconforming mesh with hanging nodes, after a one-pass refinement in the atmosphere and the basin.

5.3.2 Numerical results

The results are obtained using SDIRK(3,4) with polynomial degree $k = 3$ and time step $\Delta t = 4.7 \times 10^{-3}$ [s]. A reference solution is computed using the 2D spectral element solver of the SEM3D package (a co-developed and optimized spectral element code, <https://github.com/sem3d/SEM>), which is restricted to quadrangular meshes. This solver relies on a second-order (primal) formulation in time, an explicit Newmark scheme for time integration, with a polynomial degree $k = 4$ (using 5 GLL nodes in each tensorization direction) and a time step $\Delta t = 0.61 \times 10^{-4}$ [s]. In order to underline the significant reduction in dofs associated with static condensation in the case of an implicit time-stepping, these are reported in Table 5 for the different meshes considered before and after static condensation. The ratio of dofs reduction is about 75% on all the meshes, a value that is consistent with the estimates in Table 1.

	TYPE OF MESH			
	TRIANGULAR	QUADRANGULAR	HYBRID	NONCONFORMING
DOFS BEFORE STATIC CONDENSATION	8 538 346	4 562 532	4 533 700	3 761 468
DOFS AFTER STATIC CONDENSATION	1 448 120	977 560	971 416	810 344

Tab. 5: Number of dofs for different meshes, before and after static condensation.

Figure 16 displays the two-dimensional pressure field in the fluid subdomain and the Euclidian norm of the velocity field in the solid subdomain at the times $t \in \{0, 0.16, 0.6, 1\}$ [s]. As expected, seismoacoustics coupling happens where the mountain is located (snapshot at $t = 0.16$ [s]): The pressure wave mainly results from the direct transmission of the solid velocity pulse above the mountain, but is also related to inhomogeneous waves that are guided along the interface (lateral head waves). The seismic energy also penetrates the Eastern part of the sedimentary basin. This part of the energy is then trapped in the sedimentary basin (because of differences in impedances with the bedrock), goes back and forth and continuously couples with the atmosphere (snapshots

at times $t \in \{0.6, 1\}$ [s]). Long after its initial excitation, the basin still leaks energy into the atmosphere, as reported in [5].

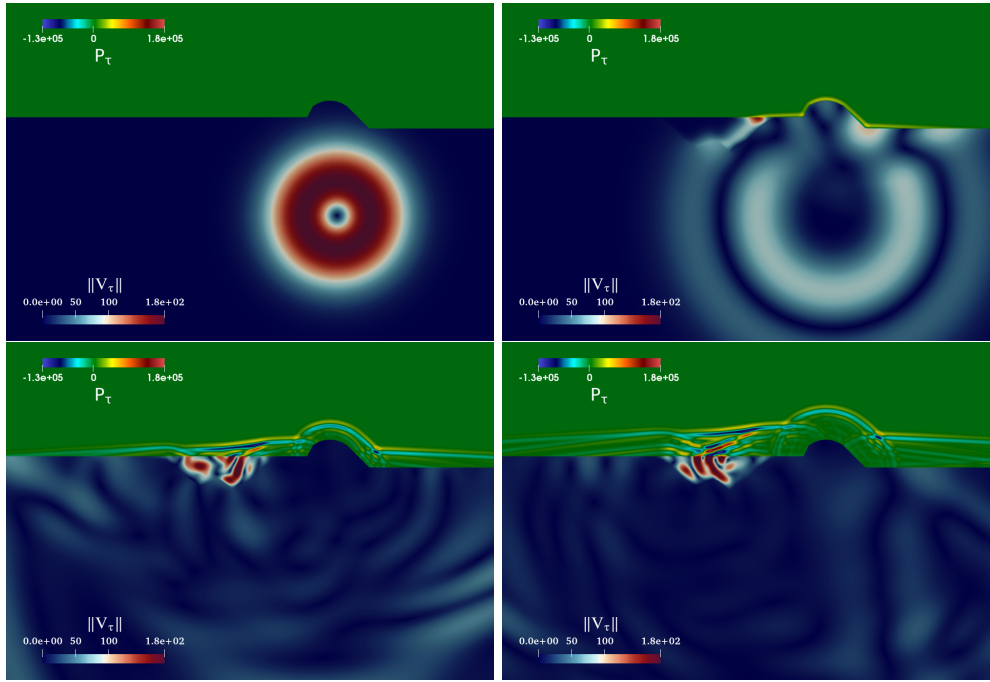


Fig. 16: Spatial distribution of the acoustic pressure (atmosphere) and the elastic velocity norm (solid subdomain) at $t \in \{0, 0.16, 0.6, 1\}$ [s]. A part of the seismic energy leaks into the atmosphere where the mountain is located; another part is trapped in the sedimentary basin, which continuously emits waves to the atmosphere.

In Figure 17, we compare the solution obtained using the HHO discretization with the reference solution at the two sensors located at $\mathcal{S}^F := (-0.65, 1.3)$ [km] and $\mathcal{S}^S := (-0.75, 1.08)$ [km]. An important conclusion is that the numerical results obtained using the HHO discretization applied to the different meshes are undistinguishable, thereby confirming the robustness of the proposed method with respect to the mesh. Furthermore, the numerical predictions perfectly match the reference solution for which the mesh is (and can only be) quadrangular. This underlines the accuracy of the developed HHO method for the simulation of wavefield propagation in complex media, and its strong potential for extension to large-scale simulations. Moreover, it is interesting to notice the oscillations in the atmosphere, that are related to the multiple waves leaking from the sedimentary basin, as seen in Figure 16.

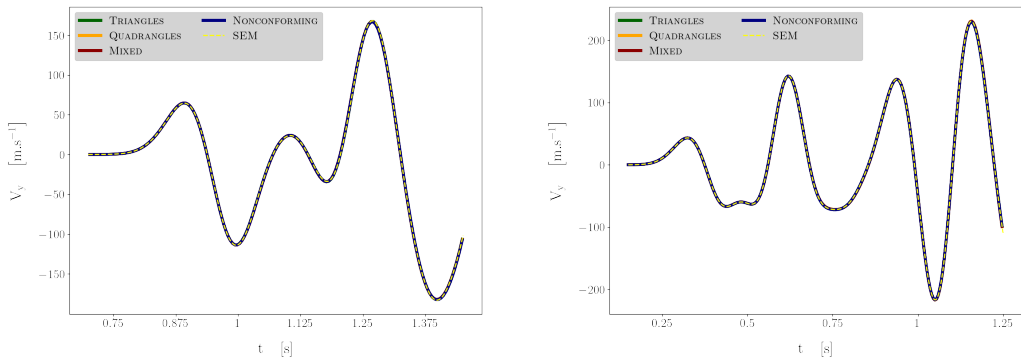


Fig. 17: Evolution of the vertical component of the velocity as a function of time. **Left:** Record at the S^F sensor, in the atmosphere. **Right:** Record at the S^S sensor, in the sedimentary basin.

6 Conclusion

We proposed a HHO method for coupled elasto-acoustic wave propagation, combining first-order formulations in time with explicit and implicit Runge–Kutta schemes. Static condensation significantly reduces computational costs in both cases. A CFL stability condition was derived numerically, and comparisons showed good performances, with implicit schemes favored. Numerical experiments confirmed the accuracy and robustness of the proposed methodology on hybrid and nonconforming meshes, including realistic seismic scenarios.

A natural extension of this work consists in coupling the HHO discretization with SEM, leveraging the geometric flexibility of HHO in complex regions while exploiting the efficiency of the SEM in the bulk where structured meshes can be used. This combined approach would enable realistic, large-scale 3D geophysical simulations to be performed. Transitioning to three dimensions will also require significant numerical and computational developments, including parallelization and possibly GPU acceleration to align with emerging exascale architectures. Such efforts will likely necessitate a renewed performance analysis, in the spirit of [35]. In parallel, further improvements such as structure-preserving time integrators (see [49, 50] for HDG space semi-discretizations) and superconvergent post-processing tailored to HHO can be explored to enhance long-time accuracy. The use of alternative polynomial bases will also be investigated as a possible means to improve accuracy and computational efficiency. Finally, an HHO-based approach combined with adaptive mesh refinement would be particularly well-suited for wave propagation problems. It could leverage the polyhedral flexibility of the method to allow for nonconforming, locally refined meshes, thereby enhancing accuracy in regions with high solution gradients while controlling computational costs.

References

- [1] K. Aki and P. Richards. *Quantitative seismology*. University Science Books, Melville, NY, 2002.
- [2] P. F. Antonietti, F. Bonaldi, and I. Mazzieri. A high-order discontinuous Galerkin approach to the elasto-acoustic problem. *Comput. Methods Appl. Mech. Engrg.*, 358:112634, 29, 2020.
- [3] P. F. Antonietti, F. Bonaldi, and I. Mazzieri. Simulation of three-dimensional elastoacoustic wave propagation based on a discontinuous Galerkin spectral element method. *Internat. J. Numer. Methods Engrg.*, 121(10):2206–2226, 2020.
- [4] S. Arrowsmith, J. Johnson, D. Drob, and M. Hedlin. The seismoacoustic wavefield: A new paradigm in studying geophysical phenomena. *Rev Geophys.*, 48:RG4003, 2010.
- [5] J. Assink, G. Averbach, S. Shani-Kadmiel, P. Smets, and L. Evers. A seismo-acoustic analysis of the 2017 North Korean nuclear test. *Seismol. Res. Lett.*, 89(6):2025–2033, 2018.
- [6] E. Burman, O. Duran, and A. Ern. Hybrid high-order methods for the acoustic wave equation in the time domain. *Commun. Appl. Math. Comput.*, 4(2):597–633, 2022.
- [7] E. Burman, O. Duran, and A. Ern. Unfitted hybrid high-order methods for the wave equation. *Comput. Methods Appl. Mech. Engrg.*, 389:Paper No. 114366, 23, 2022.
- [8] E. Chaljub, Y. Capdeville, and J.-P. Vilotte. Solving elastodynamics in a fluid-solid heterogeneous sphere: A parallel spectral element approximation on non-conforming grids. *J. Comput. Phys.*, 187(2):457–491, 2003.

- [9] E. Chaljub, P. Moczo, S. Tsuno, P.-Y. Bard, J. Kristek, M. Käser, M. Stupazzini, and M. Kris-tekova. Quantitative comparison of four numerical predictions of 3d ground motion in the Grenoble valley, France. *Bull. Seismol. Soc. Am.*, 100(4):1427–1455, 2010.
- [10] E. Chaljub and B. Valette. Spectral element modelling of three-dimensional wave propagation in a self-gravitating Earth with an arbitrarily stratified outer core. *Geophys. J. Int.*, 158(1):131–141, 2004.
- [11] I.-Y. Che, K. Kim, A. Le Pichon, J. Park, S. Arrowsmith, and B. Stump. Illuminating the North Korean nuclear explosion test in 2017 using remote infrasound observations. *Geophys. J. Int.*, 228(1):308–315, 2021.
- [12] M. Ciccuttin, D. A. Di Pietro, and A. Ern. Implementation of discontinuous skeletal methods on arbitrary-dimensional, polytopal meshes using generic programming. *J. Comput. Appl. Math.*, 344:852–874, 2018.
- [13] M. Ciccuttin, A. Ern, and N. Pignet. *Hybrid high-order methods—a primer with applications to solid mechanics*. SpringerBriefs in Mathematics. Springer, Cham, 2021.
- [14] B. Cockburn, D. A. Di Pietro, and A. Ern. Bridging the hybrid high-order and hybridizable discontinuous Galerkin methods. *ESAIM Math. Model. Numer. Anal.*, 50(3):635–650, 2016.
- [15] B. Cockburn, Z. Fu, A. Hungria, L. Ji, M. A. Sánchez, and F.-J. Sayas. Stormer-Numerov HDG methods for acoustic waves. *J. Sci. Comput.*, 75(2):597–624, 2018.
- [16] B. Cockburn, J. Gopalakrishnan, and R. Lazarov. Unified hybridization of discontinuous Galerkin, mixed, and continuous Galerkin methods for second order elliptic problems. *SIAM J. Numer. Anal.*, 47(2):1319–1365, 2009.
- [17] B. Cockburn and V. Quenneville-Bélair. Uniform-in-time superconvergence of the HDG methods for the acoustic wave equation. *Math. Comp.*, 83(285):65–85, 2014.
- [18] G. C. Cohen, P. Joly, J. E. Roberts, and N. Tordjman. Higher order triangular finite elements with mass lumping for the wave equation. *SIAM J. Numer. Anal.*, 38(6):2047–2078, 2001.
- [19] F. Dassi, A. Fumagalli, I. Mazzieri, A. Scotti, and G. Vacca. A virtual element method for the wave equation on curved edges in two dimensions. *J. Sci. Comput.*, 90(1), 2022.
- [20] J. de Basabe, J. Sen, and M. Wheeler. The interior penalty discontinuous Galerkin method for elastic wave propagation: grid dispersion. *Geophys. J. Int.*, 175(1):83–93, 2008.
- [21] E. Delavaud. Simulation numérique de la propagation d’ondes en milieu géologique complexe : application à l’évaluation de la réponse sismique du bassin de Caracas (Venezuela). *Univ. Paris VII Denis Diderot*, 2007.
- [22] D. A. Di Pietro and J. Droniou. *The hybrid high-order method for polytopal meshes*, volume 19 of *MS&A. Modeling, Simulation and Applications*. Springer, Cham, 2020.
- [23] D. A. Di Pietro and A. Ern. A hybrid high-order locking-free method for linear elasticity on general meshes. *Comput. Methods Appl. Mech. Engrg.*, 283:1–21, 2015.
- [24] D. A. Di Pietro, A. Ern, and S. Lemaire. An arbitrary-order and compact-stencil discretization of diffusion on general meshes based on local reconstruction operators. *Comput. Methods Appl. Math.*, 14(4):461–472, 2014.

- [25] J. Diaz and P. Joly. Robust high order non-conforming finite element formulation for time domain fluid-structure interaction. *J. Comput. Acoust.*, 13(3):403–431, 2005.
- [26] M. Dumbser and M. Käser. An arbitrary high-order discontinuous Galerkin method for elastic waves on unstructured meshes - II. The three-dimensional isotropic case. *Geophys. J. Int.*, 167(1):319–336, 2006.
- [27] A. Ern and R. Khot. Explicit Runge-Kutta schemes with hybrid high-order methods for the wave equation in first order form. *HAL-04763478*, 2024.
- [28] A. Ern and M. Steins. Convergence analysis for the wave equation discretized with hybrid methods in space (HHO, HDG and WG) and the leapfrog scheme in time. *J. Sci. Comput.*, 101(1):28, 2024.
- [29] A. Fichtner, B. L. N. Kennett, V. C. Tsai, C. H. Thurber, A. J. Rodgers, C. Tape, N. Rawlinson, R. D. Borcherdt, S. Lebedev, K. Priestley, C. Morency, E. Bozdağ, J. Tromp, J. Ritsema, B. Romanowicz, Q. Liu, E. Golos, and F. Lin. Seismic tomography 2024. *Bull. Seismol. Soc. Am.*, 114(3):1185–1213, 2024.
- [30] M. J. Grote, A. Schneebeli, and D. Schötzau. Discontinuous Galerkin finite element method for the wave equation. *SIAM J. Numer. Anal.*, 44(6):2408–2431, 2006.
- [31] V. Hermann, M. Käser, and C. E. Castro. Non-conforming hybrid meshes for efficient 2-d wave propagation using the discontinuous galerkin method. *Geophysical Journal International*, 184(2):746–758, 2011.
- [32] B. Hernandez, A. Le Pichon, J. Vergoz, P. Herry, L. Ceranna, C. Pilger, E. Marchetti, M. Ripepe, and R. Bossu. Estimating the ground-motion distribution of the 2016 mw 6.2 Amatrice, Italy, Earthquake using remote infrasound observations. *Seismol. Res. Lett.*, 89(6):2227–2236, 09 2018.
- [33] D. Komatitsch, C. Barnes, and J. Tromp. Wave propagation near a fluid-solid interface: A spectral-element approach. *Geophys.*, 65(2):623–631, 2000.
- [34] D. Komatitsch and J.-P. Vilotte. The Spectral Element Method: an effective tool to simulate the seismic response of 2D and 3D geological structures. *Bull. Seism. Soc. Am.*, 88:368–392, 1998.
- [35] M. Kronbichler, S. Schoeder, C. Müller, and W. A. Wall. Comparison of implicit and explicit hybridizable discontinuous Galerkin methods for the acoustic wave equation. *Internat. J. Numer. Methods Engrg.*, 106(9):712–739, 2016.
- [36] T. Lay and T. C. Wallace. *Modern global seismology*, volume 58. Academic Press, CA, 1995.
- [37] A. Léger and M. Deschamps. *Ultrasonic Wave Propagation in non homogeneous media*. Springer Berlin, Heidelberg, 2009.
- [38] C. Lehrenfeld. *Hybrid discontinuous Galerkin methods for incompressible flow problems*. Diploma thesis, CCESMath/IGPM RWTH, Aachen, 2010.
- [39] K. J. Marfurt. Accuracy of finite-difference and finite-element modelling of the scalar and elastic wave equations. *Geophys.*, 49:533–549, 1984.
- [40] Y. Masson. Distributional finite-difference modelling of seismic waves. *Geophys. J. Int.*, 233(1):264–296, 2022.

- [41] I. Mazzieri and F. Rapetti. Dispersion analysis of triangle-based spectral element methods for elastic wave propagation. *Numer. Algorithms*, 60(4):631–650, 2012.
- [42] E. Mercerat, J.-P. Vilotte, and F. Sánchez-Sesma. Triangular spectral element simulation of 2d elastic wave propagation using unstructured triangular grids. *Geophys. J. Int.*, 166(2):679–698, 2006.
- [43] E. D. Mercerat and N. Glinsky. A nodal high-order discontinuous Galerkin method for elastic wave propagation in arbitrary heterogeneous media. *Geophys. J. Int.*, 201(2):1101–1118, 2015.
- [44] P. Moczo, J. Kristek, and M. Galis. *The finite-difference modelling of earthquake motions: Waves and ruptures*. Cambridge University Press, Cambridge, 2014.
- [45] R. Mottier, A. Ern, R. Khot, and L. Guillot. Hybrid high-order methods for elasto-acoustic wave propagation in the time domain. 2025. <http://arxiv.org/abs/2502.10870>.
- [46] N. C. Nguyen, J. Peraire, and B. Cockburn. High-order implicit hybridizable discontinuous Galerkin methods for acoustics and elastodynamics. *J. Comput. Phys.*, 230(10):3695–3718, 2011.
- [47] A. Patera. A spectral element method for fluid dynamics: laminar flow in a channel expansion. *J. Comput. Phys.*, 54:468–488, 1984.
- [48] N. A. Petersson and B. Sjögreen. High order accurate finite difference modeling of seismo-acoustic wave propagation in a moving atmosphere and a heterogeneous Earth model coupled across a realistic topography. *J. Sci. Comput.*, 74(1):290–323, 2018.
- [49] M. A. Sánchez, C. Ciuca, N. C. Nguyen, J. Peraire, and B. Cockburn. Symplectic Hamiltonian HDG methods for wave propagation phenomena. *J. Comput. Phys.*, 350:951–973, 2017.
- [50] M. A. Sánchez, B. Cockburn, N.-C. Nguyen, and J. Peraire. Symplectic Hamiltonian finite element methods for linear elastodynamics. *Comput. Methods Appl. Mech. Engrg.*, 381:Paper No. 113843, 23, 2021.
- [51] M. Steins, A. Ern, O. Jamond, and F. Druí. Time-explicit hybrid high-order method for the nonlinear acoustic wave equation. *ESAIM Math. Model. Numer. Anal.*, 57(5):2977–3006, 2023.
- [52] T. L. Szabo. *Diagnostic ultrasound imaging: inside out*. Elsevier, Oxford, 2014.
- [53] S. Terrana, J. P. Vilotte, and L. Guillot. A spectral hybridizable discontinuous Galerkin method for elastic-acoustic wave propagation. *Geophys. J. Int.*, 213(1):574–602, 2017.
- [54] J. Virieux. P-SV wave propagation in heterogeneous media: Velocity-stress finite-difference method. *Geophys.*, 51(4):889–901, 1986.
- [55] L. C. Wilcox, G. Stadler, C. Burstedde, and O. Ghattas. A high-order discontinuous Galerkin method for wave propagation through coupled elastic-acoustic media. *J. Comput. Phys.*, 229(24):9373–9396, 2010.
- [56] R. Ye, M. V. de Hoop, C. L. Petrovitch, L. J. Pyrak-Nolte, and L. C. Wilcox. A discontinuous Galerkin method with a modified penalty flux for the propagation and scattering of acousto-elastic waves. *Geophys. J. Int.*, 205(2):1267–1289, 2016.